The Astrophysical Journal, 903:51 (30pp), 2020 November 1 https://doi.org/10.3847/1538-4357/abb36d

The Sloan Digital Sky Survey Reverberation Mapping Project: How Broad Emission Line Widths Change When Luminosity Changes

Shu Wang[1,2,3], Yue Shen[3,4,17], Linhua Jiang[1,2], C. J. Grier[5,6,7], Keith Horne[8], Y. Homayouni[9],
B. M. Peterson[10,11,12], Jonathan R. Trump[13], W. N. Brandt[5,6,14], P. B. Hall[15], Luis C. Ho[1,2], Jennifer I-Hsiu Li[3],
J. V. Hernandez Santisteban[8], K. Kinemuchi[16], Ian D. McGreer[7], and D. P. Schneider[5,6]

[1] Kavli Institute for Astronomy and Astrophysics, Peking University, Beijing 100871, People's Republic of China; wangshukiaa@pku.edu.cn, jiangKIAA@pku.edu.cn
[2] Department of Astronomy, School of Physics, Peking University, Beijing 100871, People's Republic of China
[3] Department of Astronomy, University of Illinois at Urbana-Champaign, Urbana, IL 61801, USA
[4] National Center for Supercomputing Applications, University of Illinois at Urbana-Champaign, Urbana, IL 61801, USA
[5] Department of Astronomy and Astrophysics, Eberly College of Science, The Pennsylvania State University, 525 Davey Laboratory, University Park, PA 16802, USA
[6] Institute for Gravitation & the Cosmos, The Pennsylvania State University, University Park, PA 16802, USA
[7] Steward Observatory, The University of Arizona, 933 North Cherry Avenue, Tucson, AZ 85721, USA
[8] SUPA Physics and Astronomy, University of St. Andrews, Fife, KY16 9SS, Scotland, UK
[9] Department of Physics, University of Connecticut, 2152 Hillside Road Unit 3046, Storrs, CT 06269, USA
[10] Department of Astronomy, The Ohio State University, 140 W 18th Avenue, Columbus, OH 43210, USA
[11] Center for Cosmology and AstroParticle Physics, The Ohio State University, 191 West Woodruff Avenue, Columbus, OH 43210, USA
[12] Space Telescope Science Institute, 3700 San Martin Drive, Baltimore, MD 21218, USA
[13] Department of Physics, University of Connecticut, 2152 Hillside Road, Unit 3046, Storrs, CT 06269, USA
[14] Department of Physics, The Pennsylvania State University, University Park, PA 16802, USA
[15] Department of Physics and Astronomy, York University, Toronto, ON M3J 1P3, Canada
[16] Apache Point Observatory and New Mexico State University, P.O. Box 59, Sunspot, NM 88349-0059, USA

Received 2020 June 10; revised 2020 August 25; accepted 2020 August 26; published 2020 October 30

Abstract

Quasar broad emission lines are largely powered by photoionization from the accretion continuum. Increased central luminosity will enhance line emissivity in more distant clouds, leading to increased average distance of the broad-line-emitting clouds and decreased averaged line width, which is known as the "breathing" broad-line region. However, different lines breathe differently, and some high-ionization lines, such as C IV, can even show "anti-breathing" where the line broadens when luminosity increases. Using multi-year photometric and spectroscopic monitoring data from the Sloan Digital Sky Survey Reverberation Mapping project, we quantify the breathing effect ($\Delta \log W = \alpha \Delta \log L$) of broad H$\alpha$, H$\beta$, Mg II, C IV, and C III] for statistical quasar samples over $z \approx 0.1$–2.5. We find that Hβ displays the most consistent normal breathing expected from the virial relation ($\alpha \sim -0.25$), Mg II and Hα on average show no breathing ($\alpha \sim 0$), and C IV (and similarly C III] and Si IV) mostly shows anti-breathing ($\alpha > 0$). The anti-breathing of C IV can be well understood by the presence of a non-varying core component in addition to a reverberating broad-base component, which is consistent with earlier findings. The deviation from canonical breathing introduces extra scatter (a luminosity-dependent bias) in single-epoch virial BH mass estimates due to intrinsic quasar variability, which underlies the long-argued caveats of C IV single-epoch masses. Using the line dispersion instead of FWHM leads to fewer, albeit still substantial, deviations from canonical breathing in most cases. Our results strengthen the need for reverberation mapping to provide reliable quasar BH masses and to quantify the level of variability-induced bias in single-epoch BH masses based on various lines.

Unified Astronomy Thesaurus concepts: Reverberation mapping (2019); Quasars (1319); Supermassive black holes (1663)

1. Introduction

Reverberation mapping studies of broad-line Active Galactic Nuclei (AGNs) have revealed a "breathing" mode of the broad Balmer lines such that when luminosity increases, the average (i.e., line-emissivity-weighted) BLR size increases and the average line width decreases (e.g., Gilbert & Peterson 2003; Denney et al. 2009; Park et al. 2012; Barth et al. 2015; Runco et al. 2016). This observation is consistent with the expectation from photoionization (e.g., Korista & Goad 2004; Cackett & Horne 2006), where the responsivity of the line emission depends on the radial distributions of incident ionizing flux and cloud densities. However, most of these results are based on Hβ and Hα targeted in previous RM programs. The RM results of other strong broad emission lines (e.g., C IV and Mg II) are scarce but recent observations of the variability of broad C IV and Mg II for distant quasars revealed different results: Mg II appears to have much weaker breathing than broad Hβ (e.g., Shen 2013; Homan et al. 2020; Yang et al. 2020) and the C IV width appears to increase when luminosity increases (e.g., Richards et al. 2002; Wilhite et al. 2006; Shen et al. 2008; Sun et al. 2018), which is in the opposite sense of breathing. These different behaviors of breathing for different broad lines suggest different distributions of the line-emitting clouds within the BLR and likely also different kinematic structures from viralized motion, such as winds and outflows. For example, previous photoionization calculations have shown

---

[17] Alfred P. Sloan Research Fellow.

Table 1
Sample Summary

RMID	SDSS−Identifier	z	L_{Bol} (erg s^{-1})	SNR$_{\mathrm{Var,con}}$	Line Name	Line SNR	τ (rest-frame)	τ Quality Ratings	Sample	Source	g-band F_Host
Hα, Hβ, and Mg II sample											
016	J141606.95+530929.8	0.850	45.563	4.06	Hβ	5.44	$32.0^{+11.6}_{-15.5}$	3	Lag0	G17	⋯
					Mg II	7.85			Lag1	G17	
017	J141324.28+530527.0	0.457	44.875	4.30	Hα	4.99	$56.6^{+7.3}_{-15.1}$	5	Lag0	G17	0.34
					Hβ	4.99	$25.5^{+10.9}_{-5.8}$	4	Lag0	G17	0.34
					Mg II	6.90			Lag1	G17	
044	J141622.83+531824.3	1.233	45.626	2.09	Mg II	4.85	$65.8^{+18.8}_{-4.8}$	G	Lag0	H20	⋯
088	J141151.78+525344.1	0.517	44.963	2.28	Hα	4.79	$54.8^{+2.9}_{-5.1}$	3	Lag0	G17	0.12
					Hβ	6.70			Lag1	G17	
					Mg II	5.09			Lag1	G17	
101	J141214.20+532546.7	0.458	45.351	2.41	Hβ	15.88	$21.4^{+4.2}_{-6.4}$	5	Lag0	G17	0.17
					Hα	20.62			Lag1	G17	
					Mg II	8.50			Lag1	G17	
160	J141041.25+531849.0	0.360	44.508	3.61	Hα	18.42	$21.0^{+1.4}_{-2.8}$	4	Lag0	G17	0.18
					Hβ	18.42	$21.9^{+4.2}_{-2.4}$	3	Lag0	G17	0.18
					Mg II	8.39			Lag1	G17	
177	J141724.59+523024.9	0.482	44.983	6.04	Hβ	6.66	$10.1^{+12.5}_{-2.7}$	4	Lag0	G17	0.21
					Hα	6.14			Lag1	G17	
					Mg II	5.03			Lag1	G17	
191	J141645.58+534446.8	0.442	44.499	2.63	Hα	2.71	$16.7^{+4.1}_{-5.5}$	4	Lag0	G17	0.40
					Hβ	2.71	$8.5^{+2.5}_{-1.4}$	5	Lag0	G17	0.40
229	J141018.04+532937.5	0.470	44.441	2.32	Hα	3.52	$22.1^{+7.7}_{-7.3}$	3	Lag0	G17	0.25
					Hβ	3.52	$16.2^{+2.9}_{-4.5}$	5	Lag0	G17	0.25
					Mg II	2.56			Lag1	G17	
252	J141751.14+522311.1	0.281	43.826	2.57	Hα	7.78	$10.1^{+2.4}_{-1.9}$	5	Lag0	G17	0.59
					Hβ	2.74			Lag1	G17	
267	J141112.72+534507.1	0.588	45.127	2.07	Hβ	5.25	$20.4^{+2.5}_{-2.0}$	5	Lag0	G17	0.21
					Mg II	9.93			Lag1	G17	
272	J141625.71+535438.5	0.263	44.850	4.66	Hα	44.93	$32.2^{+15.6}_{-12.6}$	3	Lag0	G17	0.17
					Hβ	44.93	$15.1^{+3.2}_{-4.6}$	5	Lag0	G17	0.17
300	J141941.11+533649.6	0.646	45.583	3.86	Hβ	4.35	$30.4^{+3.9}_{-8.3}$	4	Lag0	G17	0.05
					Mg II	5.33			Lag1	G17	
301	J142010.25+524029.6	0.548	44.947	6.24	Hβ	2.75	$12.8^{+5.7}_{-4.5}$	4	Lag0	G17	0.19
					Mg II	5.19			Lag1	G17	
303	J141830.20+522212.4	0.821	44.938	6.19	Mg II	5.74	$57.7^{+10.5}_{-8.3}$	G	Lag0	H20	⋯
320	J142038.52+532416.5	0.265	44.584	2.69	Hα	13.73	$20.2^{+10.5}_{-9.3}$	4	Lag0	G17	0.24
					Hβ	13.73	$25.2^{+4.7}_{-5.7}$	4	Lag0	G17	0.24
371	J141123.42+521331.7	0.473	44.909	3.19	Hα	10.79	$22.6^{+0.6}_{-1.5}$	3	Lag0	G17	0.17
					Hβ	10.79	$13.0^{+1.4}_{-0.8}$	3	Lag0	G17	0.17
					Mg II	8.55			Lag1	G17	
373	J141859.75+521809.7	0.882	45.726	3.45	Hβ	12.32	$20.4^{+5.6}_{-7.0}$	3	Lag0	G17	⋯
377	J142043.53+523611.4	0.337	44.324	2.09	Hβ	2.65	$5.9^{+0.4}_{-0.6}$	3	Lag0	G17	0.52
					Hα	8.60			Lag1	G17	
419	J141201.94+520527.6	1.272	45.761	4.07	Mg II	4.78	$95.5^{+15.2}_{-15.5}$	G	Lag0	H20	⋯
422	J140739.16+525850.7	1.074	45.418	4.33	Mg II	5.82	$109.3^{+25.4}_{-29.6}$	G	Lag0	H20	⋯
440	J142209.13+530559.7	0.754	45.646	2.61	Mg II	10.61	$114.6^{+7.4}_{-10.8}$	G	Lag0	H20	0.04
					Hβ	3.34			Lag1	H20	
449	J141941.75+535618.0	1.218	45.684	3.04	Mg II	4.63	$119.8^{+14.7}_{-24.4}$	G	Lag0	H20	⋯
459	J141206.95+540827.3	1.156	45.699	3.01	Mg II	4.23	$122.8^{+5.1}_{-5.7}$	G	Lag0	H20	⋯
589	J142049.28+521053.3	0.751	45.403	4.92	Hβ	3.91	$46.0^{+9.5}_{-9.5}$	3	Lag0	G17	0.09
					Mg II	7.73			Lag1	G17	
645	J142039.80+520359.7	0.474	44.870	5.03	Hα	7.78	$24.2^{+10.2}_{-5.3}$	5	Lag0	G17	0.11
					Hβ	7.78	$20.7^{+0.9}_{-3.0}$	4	Lag0	G17	0.11
					Mg II	3.81			Lag1	G17	
651	J142149.30+521427.8	1.486	45.896	3.64	Mg II	6.59	$76.5^{+18.0}_{-15.6}$	G	Lag0	H20	⋯
675	J140843.79+540751.2	0.919	45.791	3.41	Mg II	43.32	$139.8^{+12.0}_{-22.6}$	G	Lag0	H20	⋯
					Hβ	3.18			Lag1	H20	
694	J141706.68+514340.1	0.532	45.148	2.58	Hβ	4.66	$10.4^{+6.3}_{-3.0}$	5	Lag0	G17	0.09

Table 1
(Continued)

RMID	SDSS−Identifier	z	$L_{\rm Bol}$ (erg s^{-1})	SNR$_{\rm Var,con}$	Line Name	Line SNR	τ (rest-frame)	τ Quality Ratings	Sample	Source	g-band F_Host
709	J140855.07+515833.2	1.251	45.693	2.77	Mg II	4.33	$85.4^{+17.7}_{-19.3}$	G	Lag0	H20	⋯
714	J142349.72+523903.6	0.921	45.500	2.56	Mg II	6.50	$320.1^{+11.3}_{-11.2}$	G	Lag0	H20	⋯
756	J140923.42+515120.1	0.852	45.113	3.10	Mg II	4.08	$315.3^{+20.5}_{-16.4}$	G	Lag0	H20	⋯
761	J142412.92+523903.4	0.771	45.496	3.09	Mg II	12.19	$102.1^{+8.2}_{-7.4}$	G	Lag0	H20	0.05
					Hβ	4.56			Lag1	H20	
768	J140915.70+532721.8	0.259	44.569	5.61	Hα	21.62	$42.1^{+2.7}_{-2.1}$	5	Lag0	G17	0.57
					Hβ	6.52			Lag1	G17	
772	J142135.90+523138.9	0.249	44.273	2.42	Hα	23.13	$5.9^{+1.6}_{-1.0}$	5	Lag0	G17	0.91
					Hβ	23.13	$3.9^{+0.9}_{-0.9}$	5	Lag0	G17	0.91
775	J140759.07+534759.8	0.173	44.785	3.48	Hβ	12.58	$16.3^{+13.1}_{-6.6}$	4	Lag0	G17	⋯
					Hα	31.94			Lag1	G17	
776	J140812.09+535303.3	0.116	44.374	3.56	Hα	25.17	$8.3^{+4.9}_{-2.3}$	4	Lag0	G17	⋯
					Hβ	25.17	$10.5^{+1.0}_{-2.2}$	4	Lag0	G17	⋯
779	J141923.37+542201.7	0.152	44.164	5.92	Hβ	8.20	$11.8^{+0.7}_{-1.5}$	4	Lag0	G17	⋯
					Hα	14.95			Lag1	G17	
782	J141318.96+543202.4	0.363	44.920	3.55	Hβ	9.87	$20.0^{+1.1}_{-3.0}$	4	Lag0	G17	0.12
					Hα	20.74			Lag1	G17	
					Mg II	3.13			Lag1	G17	
790	J141729.27+531826.5	0.238	44.465	5.15	Hβ	8.43	$5.5^{+5.7}_{-2.1}$	3	Lag0	G17	0.58
					Hα	55.41			Lag1	G17	
840	J141645.15+542540.8	0.244	44.206	4.44	Hα	12.59	$10.6^{+2.3}_{-2.4}$	5	Lag0	G17	0.62
					Hβ	12.59	$5.0^{+1.5}_{-1.4}$	5	Lag0	G17	0.62
C III], C IV, and Si IV sample											
032	J141313.52+525550.2	1.715	45.475	7.05	C IV	3.55	$22.8^{+3.5}_{-3.6}$	5	Lag0	G19	⋯
145	J141818.45+524356.0	2.137	45.713	4.29	C IV	3.83	$180.9^{+4.7}_{-4.7}$	3	Lag0	G19	⋯
201	J141215.24+534312.1	1.812	46.799	6.00	C IV	16.47	$41.3^{+32.0}_{-19.5}$	3	Lag0	G19	⋯
					C III]	10.07			Lag1	G19	
231	J142005.59+530036.7	1.645	46.232	4.23	C IV	9.68	$80.4^{+6.3}_{-7.5}$	3	Lag0	G19	⋯
					C III]	7.03			Lag1	G19	
275	J140951.81+533133.7	1.577	46.181	8.45	C IV	9.78	$81.0^{+8.2}_{-24.4}$	5	Lag0	G19	⋯
295	J141347.87+521204.9	2.352	45.909	4.98	C IV	4.22	$163.8^{+8.2}_{-5.3}$	3	Lag0	G19	⋯
298	J141155.56+521802.9	1.635	46.112	2.51	C IV	5.60	$106.1^{+18.7}_{-31.7}$	4	Lag0	G19	⋯
					C III]	3.78			Lag1	G19	
387	J141905.24+535354.1	2.426	46.390	3.48	C IV	13.05	$30.3^{+19.6}_{-3.4}$	4	Lag0	G19	⋯
401	J140957.28+535047.0	1.822	46.112	3.98	C IV	11.55	$47.4^{+15.2}_{-8.9}$	4	Lag0	G19	⋯
408	J141409.85+520137.2	1.734	46.200	2.02	C IV	5.72	$178.5^{+8.2}_{-4.4}$	3	Lag0	G19	⋯
					C III]	4.82			Lag1	G19	
485	J141912.47+520818.0	2.563	46.700	2.13	C IV	6.06	$133.4^{+22.6}_{-5.2}$	3	Lag0	G19	⋯
					C III]	4.32			Lag1	G19	
					Si IV	3.17			Lag1	G19	
549	J141631.45+541719.7	2.275	45.846	3.78	C IV	4.04	$69.8^{+5.3}_{-7.2}$	4	Lag0	G19	⋯
827	J141218.03+541817.1	1.965	45.748	6.43	C IV	4.27	$137.7^{+18.3}_{-19.4}$	3	Lag0	G19	⋯

Note. The quality ratings of the lags are taken directly from the corresponding papers. H20 only provided the most reliable lags in their Gold sample, indicated by "G" in the "τ quality ratings" column.

that the broad Mg II emission comes from clouds that are on average further out than the Balmer lines in the BLR (e.g., Goad et al. 1993; O'Brien et al. 1995; Korista & Goad 2000; Goad et al. 2012). Guo et al. (2020) further suggested that, based on photoionization calculations, if most of the broad Mg II is produced near the physical outer boundary of the BLR, then Mg II will show weaker breathing than the Balmer lines. Quantifying the behaviors of breathing for different broad lines therefore offers useful constraints on the structure of the BLR and photoionization models.

In this work, we perform a detailed observational study of the BLR breathing behavior for several strong broad emission lines in quasar spectra. We quantify the general behaviors of Hβ/Hα, Mg II, C III], and C IV, in terms of breathing, using well sampled light curves that capture the continuum variability and echoed broad-line variability from the Sloan Digital Sky Survey Reverberation Mapping (SDSS-RM) project (e.g., Shen et al. 2015a). With these results, we attempt to establish an observational consensus on BLR breathing to provide valuable inputs for theoretical modeling of photoionization and kinematics of the BLR.

The structure of the paper is as follows. In Section 2, we describe the data. In Section 3, we present the results for different broad lines. We discuss our results in Section 4 and summarize in Section 5.

2. Data

The SDSS-RM project is a dedicated multi-object optical reverberation mapping program (Shen et al. 2015a) that has been spectroscopically monitoring a single 7 deg^2 field, using the SDSS Baryon Oscillation Spectroscopic Survey (BOSS, Eisenstein et al. 2011; Dawson et al. 2013) spectrographs (Smee et al. 2013) on the 2.5 m SDSS telescope (Gunn et al. 2006) at Apache Point Observatory. We also acquired accompanying photometric data in the g and i bands with the 3.6 m Canada–France–Hawaii Telescope (CFHT) and the Steward Observatory 2.3 m Bok telescope during the spectroscopic monitoring. The SDSS-RM program started in 2014 as one of the dark-time ancillary programs in SDSS-III (Eisenstein et al. 2011) and it has continued in SDSS-IV (Blanton et al. 2017).

The SDSS-RM monitoring data used in this work include the multi-epoch spectroscopy taken by the BOSS spectrographs, as well as photometric light curves from the CFHT and Bok telescopes from 2014 to 2017. The spectroscopic data were first re-processed with a custom pipeline to improve flux calibration (Shen et al. 2015a), followed by another recalibration process called PrepSpec to further improve the spectrophotometric calibration using the flux of the narrow emission lines as a constant reference (e.g., Shen et al. 2016b; Grier et al. 2017).

The SDSS-RM sample includes 849 broad-line quasars flux-limited to $i = 21.7$, covering a broad redshift range of $0.1 < z < 4.5$. In this work, we use a subset of the SDSS-RM sample that have well measured broad-line lags to examine the breathing effect. The detection of a broad-line lag ensures there is already a significant continuum variability, which facilitates the investigation of broad-line width responses. Our initial sample includes 44 SDSS-RM quasars with Hβ lag measurements (Grier et al. 2017, hereafter G17), 57 quasars with Mg II lag detections (Homayouni et al. 2020, hereafter H20) and 52 quasars with C IV lag measurements (Grier et al. 2019, hereafter G19). The imaging and spectroscopic light curves from the G17 sample cover one season (2014), and those from the G19 and H20 samples cover four seasons (2014–2017). In this work, we use the same light-curve sets from these three papers, but with several modifications (as described in Section 3.2).

Assuming a canonical $R - L$ relation (e.g., $R \propto L^{0.5}$, Bentz et al. 2013) and that the broad-line width faithfully traces the virial velocity of the BLR, the expected correlation between changes in line width ($\Delta \log W$) and continuum luminosity ($\Delta \log L$) is $\Delta \log W = -0.25 \Delta \log L$. Only objects with significant continuum variability can be used to robustly measure the breathing effect. Therefore, we first refine our initial sample using a continuum variability significance threshold. We define a continuum variability signal to noise ratio as $\mathrm{SNR}_{\mathrm{Var,con}} = \sqrt{\frac{1}{N-1} \times \sum_{i=1}^{N} (F_{\mathrm{i}} - \overline{F})^2 / F_{\mathrm{err},i}^2}$, where F_i is the g-band flux in the ith epoch, $\overline{F}$ is the average g-band flux, and N is the total number of the epochs. Compared to the SNR2 reported by Prepspec (see G17, G19, and H20), our definition is directly related to the study of $\Delta \log W - \Delta \log L$ correlation (see details in Section 3.4). We restrict our sample to objects with $\mathrm{SNR}_{\mathrm{Var,con}} > 2$, which is a good balance between sample size and $\mathrm{SNR}_{\mathrm{Var,con}}$. Choosing a more stringent criterion, such as $\mathrm{SNR}_{\mathrm{Var,con}} > 3$, the results are consistent (see details in Sections 3.4 and 3.5). Second, we require that the quality rating of the lag measurement reported in G17 and G19 is at least 3 because we will use the measured lag to synchronize the line response with continuum variability in the investigation of breathing. This criterion on lag quality is set to be slightly less stringent than that of the gold sample, which is set to be 4 in G17 and G19. Using this criterion increases the sample size by ∼30% relative to the G17 gold sample and by ∼60% relative to the G19 gold sample, while removing the least reliable lag measurements reported in G17 and G19. H20 did not report quantitative quality ratings on lag measurements but did define a gold sample. Therefore, we adopt the gold sample from H20. We will summarize our parent sample in Table 1 for further spectral analysis in Section 3.3.

To synchronize the continuum and broad line variations, we utilize the measured broad-line lags. If the specific line has a measured lag, then we simply shift the time series of the line response using the lag; for broad lines covered in the same spectrum but without reported lags, we use the lags of other lines if available (e.g., Hβ lag for Mg II, C IV lag for C III). We designate the sample with the corresponding lags the “Lag0” sample and those with substituted lags the “Lag1” sample.

3. Quantifying the Breathing Behaviors

3.1. Spectral Fitting Procedure

To perform spectral fits on the multi-epoch spectra of our sample to measure broad-line properties, we adopt the publicly available quasar spectral fitting package `QSOFIT` (Shen et al. 2019). `QSOFIT` deploys a multi-component functional fitting approach similar to earlier work (e.g., Shen et al. 2008, 2011). Its continuum model consists of a power-law, an optical Fe II template (Boroson & Green 1992), an UV Fe II template[18] (Vestergaard & Wilkes 2001; Tsuzuki et al. 2006; Salviander et al. 2007) and a 5th-order polynomial to account for any possible reddening. The emission line flux from the continuum and Fe II subtracted spectrum is then fitted with multiple Gaussians. The fits were performed in the rest-frame of the quasar using systemic redshifts from Shen et al. (2019).

`QSOFIT` allows the user to specify the fitting range and switch on/off individual continuum and line components. To mitigate the difficulty of fitting the global continuum, we fit each spectrum locally in several line complexes by specifying the `fitting range` parameter. Table 2 summarizes the fitting ranges that we use for each line complex, the continuum and line components included in the fitting, and also the number of broad-line and narrow-line Gaussians used for each line component.

We now describe the multi-epoch spectral fitting procedure in detail. For each object, we first measure the median S/N over the spectrum for all spectroscopic epochs. The mean and standard deviation σ of individual median S/N are then computed in each observing season, and epochs that are 2σ below the mean S/N of each season are rejected. This step excludes $2 \sim 6$ epochs in the 2014 season, and $0 \sim 3$ epochs in each of the other three seasons. The remaining good S/N epochs are used to generate the mean spectrum using the SDSS-III spectroscopic pipeline `idlspec2d`. Next, we fit the

---

[18] The Fe II template is the same as that used in Shen & Liu (2012). See their Section 3.1 for more details.

Table 2
Fitting Parameters

Line Complex	Fitting Range	Line Name	Line Center	$N_{\mathrm{gau},B}$[a]	$N_{\mathrm{gau},N}$[b]
Hα[c]	[6300, 6800]	Hα	6564.61	3	1
		[N II]	6549.85	0	1
			6585.28	0	1
		[S II]	6718.29	0	1
			6732.67	0	1
Hβ	[4670, 5070]	Hβ	4862.68	3	1
		He II	4687.02	1	1
		[O III]	4960.30	1	1
			5008.24	1	1
Mg II[d]	[2710, 2890]	Mg II	2795.50	3[e]	1
			2802.75		1
C III]	[1800, 2000]	C III]	1907	2	1
			1909		1
		Al III	1857.40	1	0
		Si III]	1892.03	1	0
C IV	[1500, 1703]	C IV	1548.20	3	1
			1550.77		1
		He II	1640.42	1	1
		O III]	1663.48	1	1
Si IV	[1365, 1445]	Si IV	1402.06	3	1
		O IV]	1396.76		1

Notes.
[a] The numbers of broad-line Gaussians used in the fit.
[b] The number of narrow-line Gaussians used in the fit.
[c] We do not include the Fe II component in Hα, C IV, and Si IV as the Fe II contribution in these wavelength ranges is low and often difficult to constrain.
[d] We include a 5th-order polynomial in the Mg II complex fitting because the combination of only power-law and Fe II template often provides poor fitting results.
[e] We do not set broad Gaussians separately for the Mg II doublets. The three Gaussians are for whole Mg II profile, similarly for C III], C IV and Si IV.

mean spectra using `QSOFIT`. The high S/N mean spectrum is used to obtain robust estimates of the parameters describing the narrow-line emission and the Fe II emission, which are held fixed in the multi-epoch spectra fitting. The velocity division between narrow-line and broad-line Gaussian components is set to be 450 km s^{-1} in Gaussian σ. We tie the widths of the narrow lines within the same line complex (e.g., Hβ) but allow different narrow-line widths across different line complexes (see Table 2). Fixing the Fe II emission is a simplification because broad Fe II does vary, albeit with smaller amplitude compared to other major broad lines (e.g., Barth et al. 2013; Hu et al. 2015). However, the individual epochs of spectra do not have sufficient S/N to allow reliable Fe II subtraction, and therefore we use the average Fe II emission constrained from the mean spectrum as a template to subtract this component.

As a demonstration, Figure 1 shows the multi-component functional fitting results of different line complexes from the mean spectra. Figure 2 shows the 2D residual map to illustrate the quality of the multi-epoch fitting.

3.2. Spectral Measurements

To quantify the line width, we calculate the full-width-at-half-maximum (FWHM) and the line dispersion σ_{line}, as defined in Peterson et al. (2004), from the model sum of all broad-line Gaussian components. Following the method described in Wang et al. (2019), a $[-2.5 \times \mathrm{MAD}, 2.5 \times \mathrm{MAD}]$ window is used for the calculation of σ_{line} to mitigate the adverse effects of noise and blending in the line wings. Here, MAD is the Median Absolute Deviation, which is calculated by Equation (1):

$$\mathrm{MAD} = \int |\lambda - \mathrm{MED}|\, F(\lambda) d\lambda \Big/ \int F(\lambda) d\lambda, \tag{1}$$

where MED is the median wavelength, defined as the location dividing the line in equal flux on both sides. As discussed in Wang et al. (2019), this latter approach produces σ_{line} values that are reproducible, less affected by blending issues and noisy line wings, and are adaptive to the actual line width.

We employ a Monte Carlo approach to estimate uncertainties in the line width measurements (e.g., Shen et al. 2008, 2011). We perturb the original spectrum at each pixel by a random value drawn from a zero-mean Gaussian distribution whose σ is set to the flux density uncertainty at that pixel and we obtain a mock spectrum. We apply the same fitting procedure to the mock spectrum to obtain spectral measurements. We generate 30 mock spectra per epoch of each object, and we estimate the measurement uncertainty of a spectral quantity as the semi-amplitude of the range enclosing the 16th and 84th percentiles of the distribution from the 30 trials.

In addition to the broad-line widths, we also measure the broad-line flux from our spectral fitting. We compare our flux measurements with those reported in G17, H20, and G19, which are based on PrepSpec outputs, and we find reasonable agreement (Figure 3).

In our following analysis, we use the merged g-band light curves as our baseline continuum flux, taken from G17,[19] H20 and G19. These continuum fluxes are not yet host subtracted. Park et al. (2012) found that if the host contribution is not removed in Mrk 40 (Arp 151), then it can result in much steeper slopes than the virial expectation. The reason for this is that the extra contribution from host in the continuum flux will suppress the dynamic range in luminosity variations, making the slope of the line width—continuum variability relation in log–log space steeper than the intrinsic value.

To remove the contribution of host contamination in the continuum light curves, we use the host fraction measured in Yue et al. (2018) (data obtained by private communication).[20] Yue et al. (2018) decomposed the host and nuclear light using CFHT g and i band coadded images, and measured the host fraction for 103 SDSS-RM quasars at $z < 0.8$. The host fraction is calculated within the 2″ diameter BOSS fiber and could be directly applied to spectroscopy. As listed in Table 1,

---

[19] The units of the light curves in G17 are erg s^{-1} cm^{-2} $\mathrm{Å}^{-1}$ and the flux scales are slightly adjusted in the merging process (see G17 for details). We first calculate the g-band flux of each spectroscopic epoch by convolving the PrepSpec-processed spectrum with the SDSS g-band filter curve (Doi et al. 2010) using the equation $\int f_\lambda R d\lambda \big/ \int R d\lambda$, where R is the response curve and f_λ is the flux density. Next, we scale the G17 g-band synthetic light curves to have the same mean and standard deviation as ours. We found good matches between the two sets of light curves. Finally, we perform the same re-scaling procedure on the Bok and CFHT g-band light curves.

[20] We have tested alternative estimation of the host fraction from spectral decomposition performed in Shen et al. (2015b). We found that only a few individual objects show noticeable differences, and the median values of the measured breathing effects remain more or less the same. Therefore, we conclude that our statistical results are insensitive to the detailed scheme of host correction in the continuum light curves.

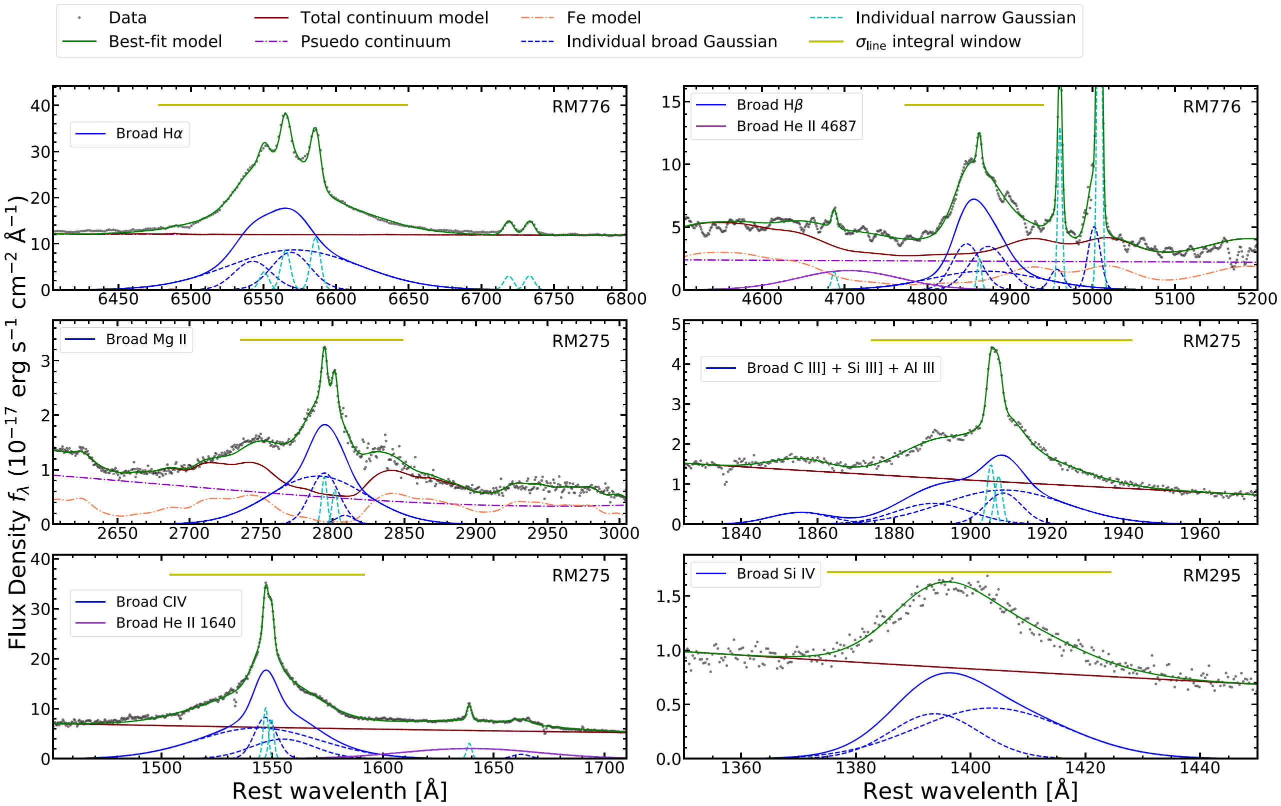

Figure 1. Examples of our multi-components functional fitting result. Each panel displays the fitting result of a line complex obtained from the coadded spectra fitting. The RMID of the object that is used to present is labeled on the top right-hand side. The continuum is re-scaled to better show the line and the continuum simultaneously. Notably, in RM275 there is strong evidence for a narrow-line component in Mg II, C III] and C IV. The horizontal line segment indicates the adaptive window that we use to calculate the line dispersion $\sigma_{\rm line}$.

the g-band host fraction $f_{{\rm host},g}$ is moderate or low for most of our objects, but could reach as high as 0.9 (RM772 at $z = 0.249$) for low-redshift objects. For objects at $z < 0.8$, we measured the g-band host flux from the mean spectrum. We convolve the mean spectrum with the g-band response curve (Doi et al. 2010) to derive the total flux, which is multiplied by the g-band host fraction to derive the host flux. The obtained g-band host flux is subtracted from the light curves as a constant offset. For objects at $z > 0.8$, we assume the host fraction is negligible in the g-band.

3.3. Final Sample

We define a line S/N to restrict the breathing analysis to the subset of quasars with reliable spectral measurements. The line S/N is calculated from the continuum model subtracted residual spectrum and defined as the ratio between the broad-line model flux and the flux uncertainty. The broad-line model flux is calculated within the velocity range of [$-2.5 \times$ MAD, $2.5 \times$ MAD] (same as the range for $\sigma_{\rm line}$ calculation). This is a better line S/N criterion than using the continuum-unsubtracted spectral S/N because we could lose some objects with large equivalent widths (EWs) but low continuum levels.

We first fit all epochs of spectra for all objects in the parent sample, and we then calculate the median line S/N from all epochs. We select our final sample by requiring the median line S/N > 2 for the G17 sample, and >3 for G19 and H20 samples. The more stringent criterion for the G19 and H20 samples is used because the multi-year observations in these two papers have a wider range of S/N variation than that for the single-season observations in G17.

In addition to the restriction on the median line S/N, we also exclude individual epochs with line S/N less than 2 in our following analysis. Table 3 summarizes the statistics of different lines covered by our final sample, and Figure 4 displays their redshift and luminosity distribution.

3.4. Hα, Hβ, and Mg II Breathing

We now examine the three major broad lines accessible in optical spectroscopy for low-redshift quasars, Hα, Hβ, and Mg II. For the normal breathing effect, we seek anti-correlations between variations of the continuum flux and line width. If the broad-line flux responds to continuum flux variations, then we can use the broad-line flux as a surrogate to track luminosity variations. The advantage of using the broad-line flux is that there is no time delay in the anti-correlation between line flux and width variations. However, the line flux light curve is much less sampled than the continuum light curve and it generally has worse S/N. Therefore, we chose to use the better sampled continuum light curve as the reference light curve, and we take into account the time lag between the continuum variability and broad-line response.

Figure 5 presents two examples of time variations of continuum flux (host subtracted, if applicable), line flux, and broad-line widths of Hα, Hβ, and Mg II. There is clear evidence of anti-correlated variations between the continuum flux $f_{\rm con}$ and the line widths (both FWHM and $\sigma_{\rm line}$) for all three lines in these two quasars (i.e., the normal breathing effect).

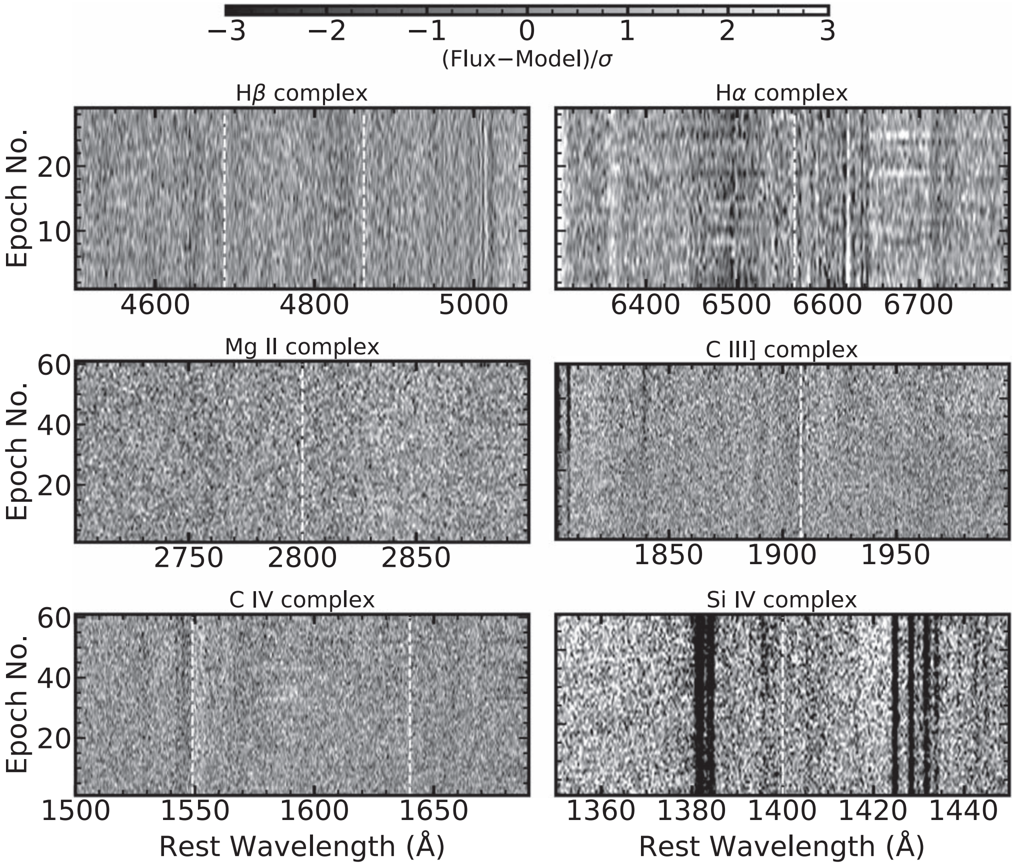

Figure 2. Examples of 2D normalized residual maps of six line complexes in individual objects. The white-dashed lines mark the locations of the primary broad emission line in each complex. These residual maps exhibit the quality of our multi-epoch fitting procedure. The dark-vertical lines in the Si IV panel are due to the strong absorption in this object.

Next, following Shen (2013), we study the changes in line width as a function of changes in continuum flux in log–log space using the following equation:

$$\Delta(\log W) = \alpha\Delta(\log f_{\rm con}) + \beta, \quad (2)$$

where W is the line width, either FWHM or $\sigma_{\rm line}$; $f_{\rm con}$ is the continuum flux; α and β are the slope and intercept. We use subscripts F and S to denote the α and β results using FWHM and $\sigma_{\rm line}$, respectively.

To synchronize each continuum light curve and the time series of line width variations, we interpolate the continuum light curve using JAVELIN (Zu et al. 2011). JAVELIN models the continuum variability of quasars assuming a Damped Random Walk (DRW) model (e.g., Kelly et al. 2009; Kozłowski et al. 2010), which provides empirical and more accurate interpolations of the light curves than using simple linear interpolations. The interpolated continuum light curves are plotted in the top panel of Figure 5. For the uncertainties of the interpolated flux, we take into account both the uncertainties reported in the JAVELIN interpolated light curves and the uncertainties of the lag measurements. For the interpolated flux uncertainty from lag measurements, we assume the true lag is uniformly distributed between $[\tau - \tau_{\rm nerr}, \tau + \tau_{\rm perr}]$, where τ, $\tau_{\rm nerr}$ and $\tau_{\rm perr}$ are the measured lag, lower and upper uncertainties of the lag, respectively. We generate 50 simulated lags within the range above and obtain the interpolated flux and flux uncertainty for each simulated lag. The final interpolated flux and uncertainty are calculated as follows:

$$f_{\rm final} = \frac{\sum_{i=1}^{50} f_i * w_i}{\sum_{i=1}^{50} w_i} \quad (3)$$

$$f_{\rm err,final} = \left(\frac{1}{50 - 1}\sum_{i=1}^{50} w_i\right)^{-0.5} \quad (4)$$

where w_i is the weight calculated by $\frac{1}{f_{{\rm err},i}^2}$. If an interpolated flux point is located in a seasonal gap, it will have larger uncertainties as showed in Figure 5.

We then pair the synchronized continuum flux and line widths at two different epochs. For each pair of epochs with synchronized line width and continuum flux, we calculate two symmetric sets of differences: $[\log f_{\rm con,1} - \log f_{\rm con,2}$, $\log W_1 - \log W_2]$ and $[\log f_{\rm con,2} - \log f_{\rm con,1}$, $\log W_2 - \log W_1]$, where subscripts 1 and 2 denote the two epochs. For an object with N pairs, we have $N(N-1)$ sets of $[\Delta(\log f_{\rm con})$, $\Delta(\log W)]$. This redundancy of data points enforces a symmetric distribution of the flux and line width changes and hence a zero intercept β. Therefore, the slope α measures the breathing effect.[21] The uncertainties of $\Delta(\log f_{\rm con})$ and $\Delta(\log W)$ are derived using error propagation from the uncertainties in $f_{\rm con}$ and W, respectively. As in Shen (2013), most points are located around zero and these small changes in

---

[21] If we do not use duplicated points in the regression, then the slope α does not change. The slope uncertainty increases by ~40%.

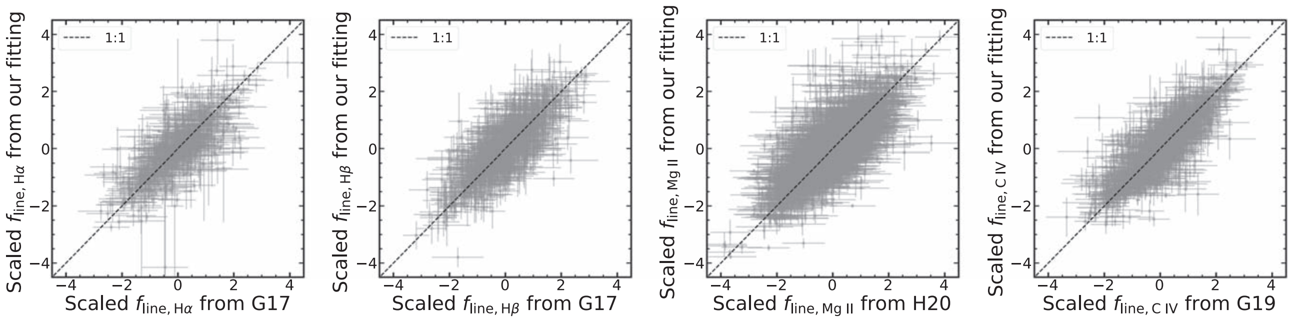

Figure 3. Comparison between our Hα, Hβ, Mg II, and C IV line flux measurements and those from PrepSpec outputs reported in G17, H20, and G19. Each gray dot with error bars is a measurement from one epoch of one object. The black-dashed line represents the 1:1 correlation. We have scaled the variable line fluxes in each light curve to have zero mean and a unity standard deviation. Our normalized line flux measurements are in good agreement with PrepSpec results.

Table 3
Sample Statistics

Line Complex	Lag0 Sample	Lag1 Sample in G17	Lag1 Sample in H20	Lag1 Sample in G19	Full Sample
Hα	14	7	0	0	21
Hβ	25	3	3	0	31
Mg II	13	15	0	0	28
C III]	0	0	0	5	5
C IV	13	0	0	0	13
Si IV	0	0	0	1	1

continuum flux and line widths are consistent with measurement uncertainties. We remove those points with absolute value of $\Delta(\log f_{\rm con})$ less than 1.5 times their uncertainties $\Delta(\log f_{\rm con,err})$. Our selection criterion of $\text{SNR}_{\rm Var,con} > 2$ almost guarantees that there are enough points left for slope measurements. There is only one object, RM392 in the H20 sample, that does not have enough points to meaningfully measure the slope after light-curve interpolation. We thus exclude this object from further analysis.

To measure the slope α between $\Delta(\log W)$ and $\Delta(\log f_{\rm con})$ we use the Bayesian linear regression package `linmix` from Kelly (2007). We also measures the Pearson correlation coefficient r between the variations in line width and continuum flux. The final results are summarized in Table 4.

We present the $\Delta(\log W) - \Delta(\log f_{\rm con})$ correlation of the three low-ionization lines in Figures 6 and 7 for the two examples shown in Figure 5. In RM840, the slopes (based on both FWHM and $\sigma_{\rm line}$) of Hβ are consistent with the expected value of -0.25 from the virial relation within 3σ uncertainties, but the slopes of Hα are shallower. In RM303, the slope based on Mg II FWHM is closer to the expected value of -0.25 than $\sigma_{\rm line}$.

We report the values of α_F and α_S for Hβ, Hα, and Mg II, measured for individual objects in our sample, in Table 4. Figure 8 displays the distributions of the two slopes for the three lines. Median (MED) slopes and their uncertainties are estimated by bootstrap resampling. We adopt the median of the bootstrap distribution and the semi-amplitude of the range enclosing the 16th and 84th percentiles as the measured MEDs and their uncertainties, respectively. In general, the Lag0 sample and the full sample (Lag0 plus Lag1 sample) show consistent MED slopes, which suggests that using the lag from an alternative line to synchronize the continuum light curve with line width changes is a reasonable approximation. We also find that the fractions of the three cases (i.e., breathing, non-detection of breathing, and anti-breathing) are similar in the Lag0 sample and the full sample for Hβ. For Mg II and Hα, the fraction of non-detections in the full sample is larger than that in the Lag0 sample. This happens because objects in the Lag1 sample generally have smaller flux variation, and Hβ is usually more variable than Hα and Mg II. The statistics of the slope distribution are summarized in Table 5. The median (MED) values of α_F and α_S for Hβ are closer to the expected value of -0.25 than for Hα and Mg II. Meanwhile, for Hβ, the slope based on $\sigma_{\rm line}$ is closer to the expected value of -0.25 than the slope based on FWHM.

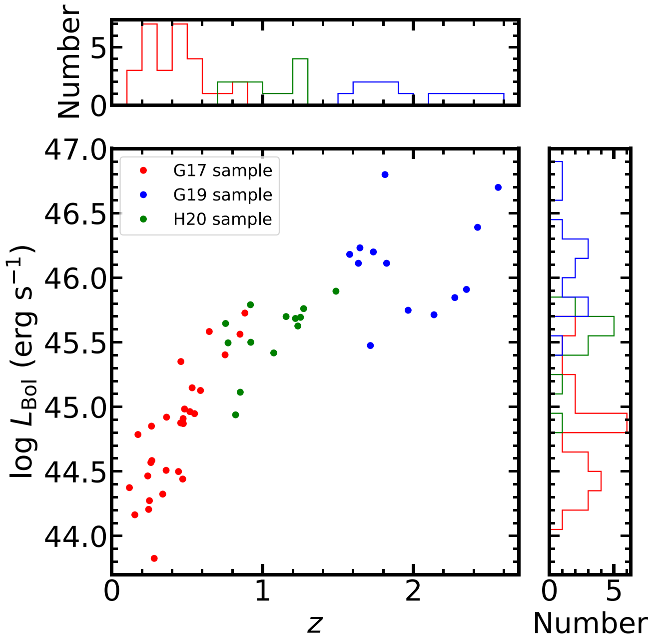

Figure 4. Distribution of quasars in our final sample for the breathing study from the G17, G19, H20 samples in the $L_{\rm Bol} - z$ plane.

While the median slope is negative, which is indicative of normal breathing to some extent, the distribution of the slope in our sample is broad for all three low-ionization lines, and some objects show a positive slope indicative of very different breathing behaviors. To quantify the different breathing behaviors, we define three breathing modes (i.e., normal breathing, no breathing and anti-breathing), as follows:

$$\text{Normal breathing:}\ \ \alpha < -3\alpha_{\rm err} \tag{5}$$

$$\text{Non}-\text{detection of breathing:}\ \ -3\alpha_{\rm err} \leqslant \alpha \leqslant 3\alpha_{\rm err} \tag{6}$$

$$\text{Anti}-\text{breathing:}\ \ \alpha > 3\alpha_{\rm err}, \tag{7}$$

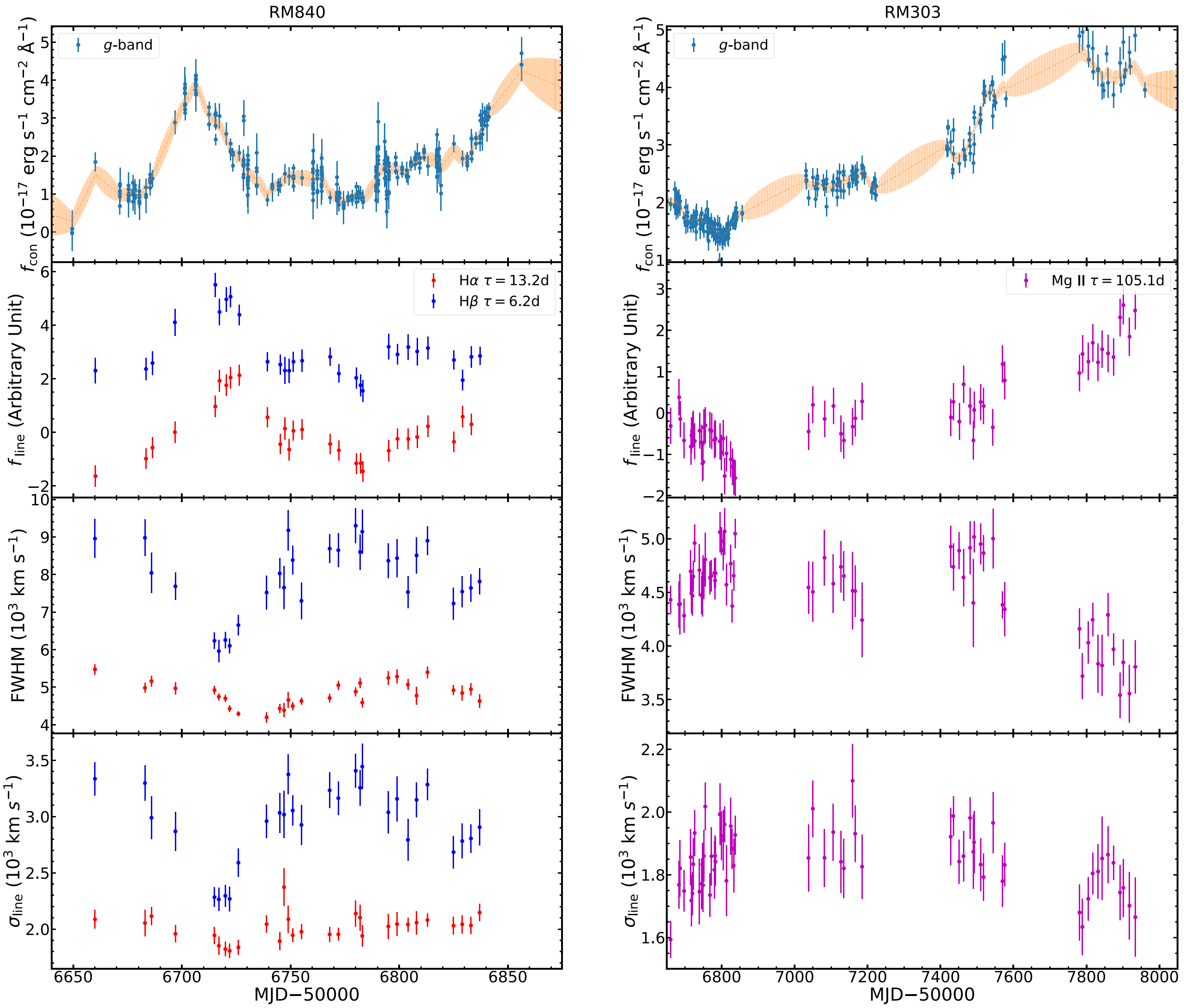

Figure 5. Two examples of time variations of continuum flux $f_{\rm con}$ (first panel), line flux (second panel), line width FWHM (third panel), and $\sigma_{\rm line}$ (fourth panel) of Hβ and Hα in the first observing season (left-hand side, RM840), and of Mg II in 2014–2017 (right-hand side, RM303). Different lines are in different colors and the observed-frame lag of each line (if reported) is also marked. $f_{\rm con}$ is the host-subtracted (if applicable) g-band flux. The line fluxes display the lag from the continuum light curves. The line fluxes are in arbitrary units and are vertically offset for clarity. There is clear evidence for normal breathing for all three low-ionization broad lines in these two quasars.

where α is either α_F or α_S, and $\alpha_{\rm err}$ is the slope uncertainty reported by `linmix`. We calculate the fractions of normal breathing, no breathing, and anti-breathing, q_-, q_0 and q_+, and we summarize the results for all three lines in Table 5. Hβ is the line that is most consistent with normal breathing. In contrast, both Mg II and Hα show a large fraction of no breathing, consistent with earlier studies (e.g., Shen 2013). Anti-breathing is rare for all three low-ionization lines. We discuss the implications of these results further in Section 4.

In our fiducial approach, we fixed the Fe II parameters in the multi-epoch spectral decomposition. The weak Fe II variability may have a non-negligible effect on the wings of the Mg II profile, which $\sigma_{\rm line}$ is more sensitive to. To test this effect, we allow the Fe II parameters to vary and refit objects included in the Mg II Lag0 sample. The median slopes in this case are -0.11 ± 0.08 and -0.02 ± 0.04, using FWHM and $\sigma_{\rm line}$, respectively, which are fully consistent with those derived in the fiducial case. Therefore, our results are insensitive to the details of treating the Fe II emission around Mg II.

Our sample includes a hypervariable quasar SDSS J141324+530527 (RM017), which is identified as a changing-look quasar in Wang et al. (2018) using spectroscopic data from the SDSS-RM project. Dexter et al. (2019) studies the response of different emission lines in terms of line flux and width to the dramatic continuum flux variation using monitoring data from 2009 to 2018. In our work, we only include the light curve in the 2014 observing season for this particular object. In 2014, RM017 showed moderate variations in the continuum flux and line width. The derived α_S for Hα, Hβ, and Mg II in this work are -0.16 ± 0.03, -0.22 ± 0.02 and -0.07 ± 0.01, which are smaller but generally consistent with the values measured in Dexter et al. (2019): -0.21 ± 0.02, -0.26 ± 0.03 and -0.12 ± 0.04, respectively.

Finally, as mentioned in Section 2, using a more strict criterion for our sample, such as $\mathrm{SNR}_{\rm Var,con} > 3$, the distributions of breathing slopes are generally consistent. We present the results derived with the samples defined by the new criterion in Figure 19. While the sample size of Hα, Hβ, and

Table 4

Breathing Effects for Hα, Hβ, and Mg II

		Hα				Hβ				Mg II			
RMID (1)	N (2)	r_F (3)	α_F (4)	r_S (5)	α_S (6)	r_F (7)	α_F (8)	r_S (9)	α_S (10)	r_F (11)	α_F (12)	r_S (13)	α_S (14)
016*	28	⋯	⋯	⋯	⋯	0.49	0.22 ± 0.03	0.15	0.07 ± 0.04	0.33	0.12 ± 0.03	0.45	0.21 ± 0.04
017	28	−0.72	−0.07 ± 0.02	−0.83	−0.16 ± 0.03	−0.80	−0.30 ± 0.03	−0.91	−0.22 ± 0.02	−0.12	−0.01 ± 0.01	−0.60	−0.07 ± 0.01
044*	62	⋯	⋯	⋯	⋯	⋯	⋯	⋯	⋯	−0.04	0.02 ± 0.06	0.56	0.25 ± 0.06
088*	28	0.43	0.21 ± 0.08	0.50	0.27 ± 0.08	0.15	0.06 ± 0.06	0.11	0.09 ± 0.07	0.14	0.14 ± 0.10	−0.16	−0.05 ± 0.08
101	29	−0.71	−0.21 ± 0.06	0.04	0.02 ± 0.12	−0.45	−0.15 ± 0.04	−0.30	−0.07 ± 0.04	−0.45	−0.18 ± 0.06	−0.46	−0.36 ± 0.09
160	29	−0.78	−0.09 ± 0.01	−0.94	−0.16 ± 0.01	−0.54	−0.08 ± 0.02	−0.57	−0.08 ± 0.01	−0.37	−0.06 ± 0.01	−0.43	−0.08 ± 0.01
177	29	−0.08	−0.05 ± 0.09	0.03	0.01 ± 0.02	−0.12	−0.06 ± 0.03	−0.65	−0.18 ± 0.03	−0.11	−0.05 ± 0.04	−0.15	−0.05 ± 0.03
191	29	−0.59	−0.24 ± 0.04	−0.25	−0.16 ± 0.05	−0.26	−0.06 ± 0.05	−0.80	−0.58 ± 0.08	⋯	⋯	⋯	⋯
229	29	−0.34	−0.14 ± 0.06	−0.19	−0.05 ± 0.07	−0.47	−0.50 ± 0.08	−0.41	−0.19 ± 0.04	0.13	0.09 ± 0.06	0.35	0.19 ± 0.06
252*	28	−0.07	−0.00 ± 0.01	−0.30	−0.02 ± 0.01	0.06	−0.02 ± 0.02	−0.13	−0.04 ± 0.02	⋯	⋯	⋯	⋯
267	28	⋯	⋯	⋯	⋯	−0.28	−0.10 ± 0.04	0.08	0.06 ± 0.06	−0.31	−0.06 ± 0.03	0.22	0.10 ± 0.05
272	29	0.12	0.02 ± 0.03	−0.05	0.02 ± 0.02	0.48	0.10 ± 0.02	0.03	−0.00 ± 0.02	⋯	⋯	⋯	⋯
300	29	⋯	⋯	⋯	⋯	−0.71	−0.74 ± 0.09	−0.41	−0.42 ± 0.10	0.03	−0.04 ± 0.14	−0.21	−0.26 ± 0.09
301	26	⋯	⋯	⋯	⋯	−0.65	−0.29 ± 0.03	−0.77	−0.28 ± 0.02	0.07	0.01 ± 0.02	0.19	0.03 ± 0.01
303*	62	⋯	⋯	⋯	⋯	⋯	⋯	⋯	⋯	−0.75	−0.19 ± 0.01	−0.43	−0.06 ± 0.01
320	29	−0.09	−0.04 ± 0.08	−0.45	−0.15 ± 0.09	−0.50	−0.38 ± 0.06	−0.66	−0.48 ± 0.06	⋯	⋯	⋯	⋯
371	29	0.05	0.07 ± 0.02	−0.50	−0.09 ± 0.02	−0.03	−0.00 ± 0.01	−0.95	−0.30 ± 0.01	−0.24	−0.05 ± 0.02	0.12	0.02 ± 0.02
373*	26	⋯	⋯	⋯	⋯	0.77	0.66 ± 0.07	0.82	0.82 ± 0.10	⋯	⋯	⋯	⋯
377	29	−0.16	−0.05 ± 0.05	−0.51	−0.25 ± 0.09	−0.10	−0.06 ± 0.10	−0.24	−0.19 ± 0.08	⋯	⋯	⋯	⋯
419*	56	⋯	⋯	⋯	⋯	⋯	⋯	⋯	⋯	0.65	0.17 ± 0.01	0.76	0.16 ± 0.01
422*	63	⋯	⋯	⋯	⋯	⋯	⋯	⋯	⋯	0.12	0.01 ± 0.01	0.20	0.02 ± 0.01
440	61	⋯	⋯	⋯	⋯	−0.88	−0.63 ± 0.03	−0.88	−0.58 ± 0.03	−0.56	−0.12 ± 0.01	0.29	−0.06 ± 0.01
449*	63	⋯	⋯	⋯	⋯	⋯	⋯	⋯	⋯	−0.38	−0.15 ± 0.03	0.10	0.04 ± 0.03
459*	60	⋯	⋯	⋯	⋯	⋯	⋯	⋯	⋯	0.05	0.00 ± 0.05	0.33	0.18 ± 0.04
589	28	⋯	⋯	⋯	⋯	−0.76	−0.22 ± 0.03	0.02	−0.03 ± 0.04	−0.70	−0.08 ± 0.01	−0.76	−0.10 ± 0.01
601	28	⋯	⋯	⋯	⋯	⋯	⋯	⋯	⋯	−0.43	−0.22 ± 0.04	−0.09	−0.03 ± 0.03
645	28	0.51	0.08 ± 0.02	−0.07	−0.04 ± 0.03	−0.49	−0.13 ± 0.02	−0.86	−0.28 ± 0.02	0.09	0.01 ± 0.02	0.21	0.08 ± 0.03
651*	64	⋯	⋯	⋯	⋯	⋯	⋯	⋯	⋯	−0.01	0.00 ± 0.01	0.00	0.00 ± 0.01
675*	58	⋯	⋯	⋯	⋯	−0.73	−0.93 ± 0.06	−0.71	−0.54 ± 0.04	−0.48	−0.23 ± 0.03	−0.35	−0.14 ± 0.03
694	29	⋯	⋯	⋯	⋯	−0.11	−0.01 ± 0.04	−0.22	−0.06 ± 0.06	⋯	⋯	⋯	⋯
709*	61	⋯	⋯	⋯	⋯	⋯	⋯	⋯	⋯	−0.36	−0.16 ± 0.05	−0.37	−0.19 ± 0.05
714*	60	⋯	⋯	⋯	⋯	⋯	⋯	⋯	⋯	−0.56	−0.28 ± 0.06	−0.60	−0.12 ± 0.04
756*	58	⋯	⋯	⋯	⋯	⋯	⋯	⋯	⋯	0.05	0.07 ± 0.09	0.78	0.31 ± 0.05
761	61	⋯	⋯	⋯	⋯	−0.64	−0.34 ± 0.03	−0.46	−0.23 ± 0.02	−0.58	−0.18 ± 0.01	−0.28	−0.07 ± 0.01
768	27	−0.82	−0.15 ± 0.02	−0.71	−0.10 ± 0.02	−0.47	−0.10 ± 0.03	−0.51	−0.12 ± 0.03	⋯	⋯	⋯	⋯
772	29	−0.91	−0.07 ± 0.01	−0.89	−0.08 ± 0.01	−0.86	−0.31 ± 0.02	−0.78	−0.21 ± 0.02	⋯	⋯	⋯	⋯
775	26	0.20	0.05 ± 0.02	−0.07	−0.07 ± 0.03	0.46	0.13 ± 0.02	−0.83	−0.33 ± 0.02	⋯	⋯	⋯	⋯
776	29	−0.37	−0.16 ± 0.04	−0.43	−0.36 ± 0.06	−0.66	−0.41 ± 0.04	−0.80	−0.87 ± 0.05	⋯	⋯	⋯	⋯
779	29	0.21	0.02 ± 0.01	−0.78	−0.06 ± 0.02	−0.08	0.01 ± 0.01	−0.84	−0.19 ± 0.01	⋯	⋯	⋯	⋯
782	29	−0.01	−0.01 ± 0.08	0.53	0.40 ± 0.22	−0.09	−0.02 ± 0.10	−0.76	−0.60 ± 0.09	⋯	⋯	⋯	⋯
790	29	0.21	0.42 ± 0.18	−0.27	−0.06 ± 0.21	−0.52	−0.10 ± 0.02	−0.50	−0.08 ± 0.01	⋯	⋯	⋯	⋯
840	29	−0.50	−0.06 ± 0.01	−0.59	−0.07 ± 0.01	−0.86	−0.28 ± 0.01	−0.89	−0.28 ± 0.01	⋯	⋯	⋯	⋯

Note. Column (1): SDSS-RM identifier RMID; * indicates an object where host measurements are unavailable; (2): Number of epochs used for spectral analysis; (3)–(4): Pearson correlation coefficient r and slopes in the $\Delta \log W - \Delta \log L$ relation derived using FWHM for Hα; (5)–(6): Pearson correlation coefficient r and slopes in the $\Delta \log W - \Delta \log L$ relation derived using $\sigma_{\rm line}$; (7)–(10): same as (3)–(6) but for Hβ; (11)–(14): same as (3)–(6) but for Mg II.

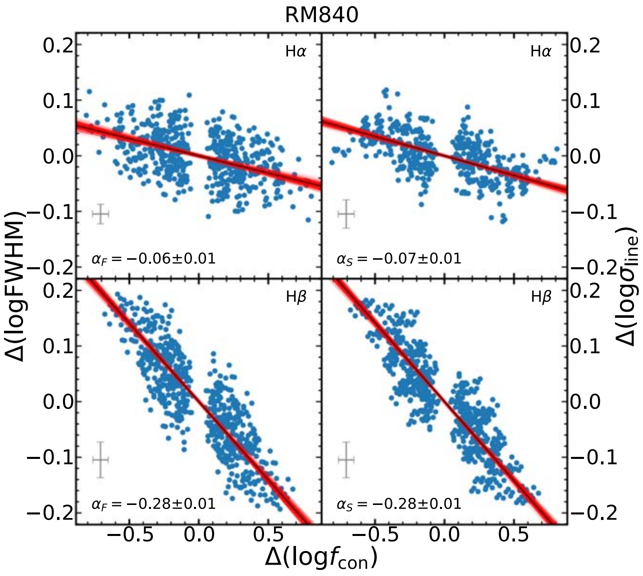

Figure 6. $\Delta\log W - \Delta\log L$ correlations for Hα and Hβ in RM840 in the first observing season of SDSS-RM. For g-band continuum flux $f_{\rm con}$, we use the host-subtracted flux. The left-hand two panels present the results of FWHM while the right-hand two panels are for $\sigma_{\rm line}$. The black-solid lines and the red-shaded regions are the median and 1σ confidence ranges of the regression fit, respectively, derived from the Bayesian linear regression package `linmix` (Kelly 2007). The gray pluses represent the median uncertainties along both axes.

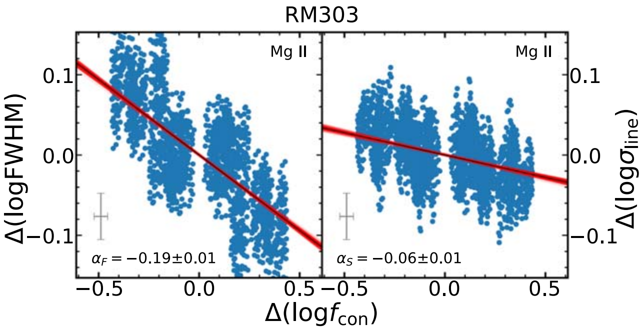

Figure 7. The $\Delta\log W - \Delta\log L$ correlation of RM303 for Mg II during the 2014–2017 observations of SDSS-RM.

Mg II Lag0 sample decreases to 8, 17, 9 (compared to 14, 25, 13 for $\mathrm{SNR}_{\rm Var,con} > 2$), the median slopes are generally consistent within uncertainties with our fiducial results.

3.5. C IV, C III] and Si IV

We now examine the three broad lines, C IV, C III] and Si IV, covered by optical spectroscopy for high-redshift quasars. Since the timescales of continuum variability of these high-redshift quasars are longer than those in the low-redshift sample due to their higher luminosity and redshift, we use the multi-year g-band light curves compiled in H20 and G19 for this subset of SDSS-RM quasars. No host correction is available for these high-redshift ($z > 1$) quasars, but the host contamination in g-band is much smaller than their low-z counterparts and therefore does not have much impact on our results.

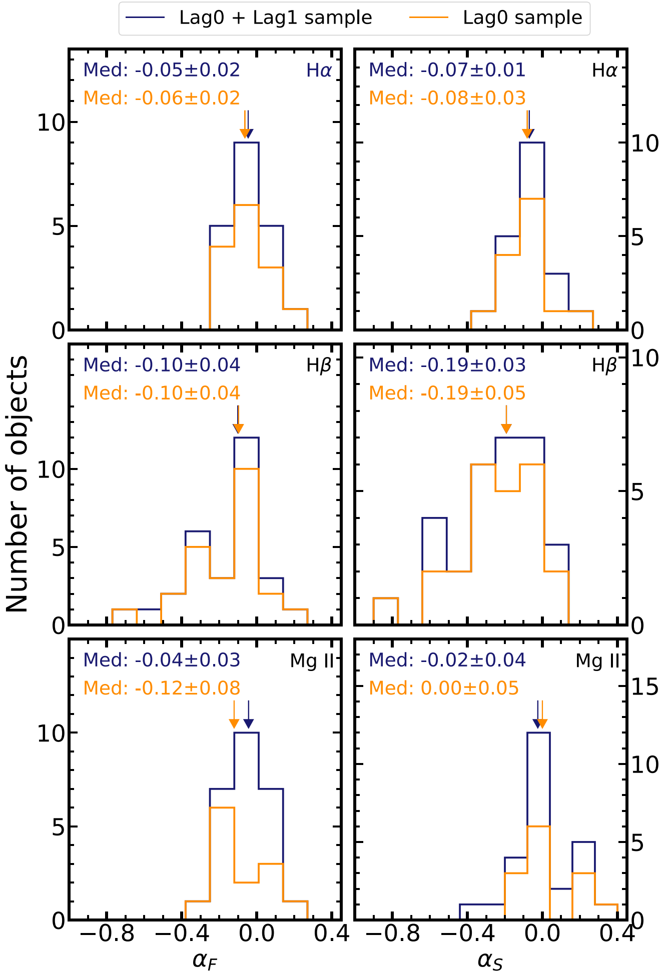

Figure 8. Distributions of the slope in the $\Delta\log W - \Delta\log L$ correlation for broad Hα, Hβ, and Mg II, and for α_F (left-hand side) and α_S (right-hand side), derived using FWHM and $\sigma_{\rm line}$, respectively.

Figure 9 presents an example with coverage of C III], C IV, and Mg II. Interestingly, C III] and C IV show anti-breathing while Mg II shows no breathing, which is expected since the Mg II line flux does not seem to respond to the drop in continuum flux either. We find that for many objects in our sample with both Mg II and C IV coverage, only C IV shows visible reverberation to continuum variations. This is a reflection of the observed fact that Mg II responds to continuum variability to a lesser extent compared to other broad lines (e.g., Goad et al. 1993; Guo et al. 2020; Yang et al. 2020).

Next, we follow the same approach in Section 3.4 to analyze the $\Delta(\log W) - \Delta(\log f_{\rm con})$ correlation for the three broad lines in high-z quasars. We present the slope constraints in Figure 10 for the same example shown in Figure 9.

We summarize the measured α_F and α_S for these three lines for all objects in our sample in Table 6. Figure 11 displays the distribution of these slopes. For most objects, α_F and α_S of C IV, as well as α_F of the C III] blends show anti-breathing. However, only a few objects also show normal breathing. There is only one object in our final sample for which we can measure for Si IV, and the inferred breathing slope is slightly positive (indicating anti-breathing) but the uncertainty is large.

Finally, we present the distributions of the breathing slope for C III] and C IV for samples defined by a more stringent

Table 5
Slope Statistics of Hα, Hβ, and Mg II Breathing

Sample Line		Lag0				Lag0 + Lag1			
		MED	q_-	q_0	q_+	MED	q_-	q_0	q_+
Hα	α_F	−0.06 ± 0.02	0.43	0.43	0.14	−0.05 ± 0.02	0.33	0.57	0.10
	α_S	−0.08 ± 0.03	0.57	0.36	0.07	−0.07 ± 0.01	0.43	0.52	0.05
Hβ	α_F	−0.10 ± 0.04	0.52	0.32	0.16	−0.10 ± 0.04	0.55	0.32	0.12
	α_S	−0.19 ± 0.05	0.68	0.28	0.04	−0.19 ± 0.03	0.68	0.29	0.03
Mg II	α_F	−0.12 ± 0.08	0.46	0.46	0.08	−0.04 ± 0.03	0.31	0.62	0.07
	α_S	−0.00 ± 0.05	0.46	0.15	0.38	−0.02 ± 0.04	0.38	0.35	0.29

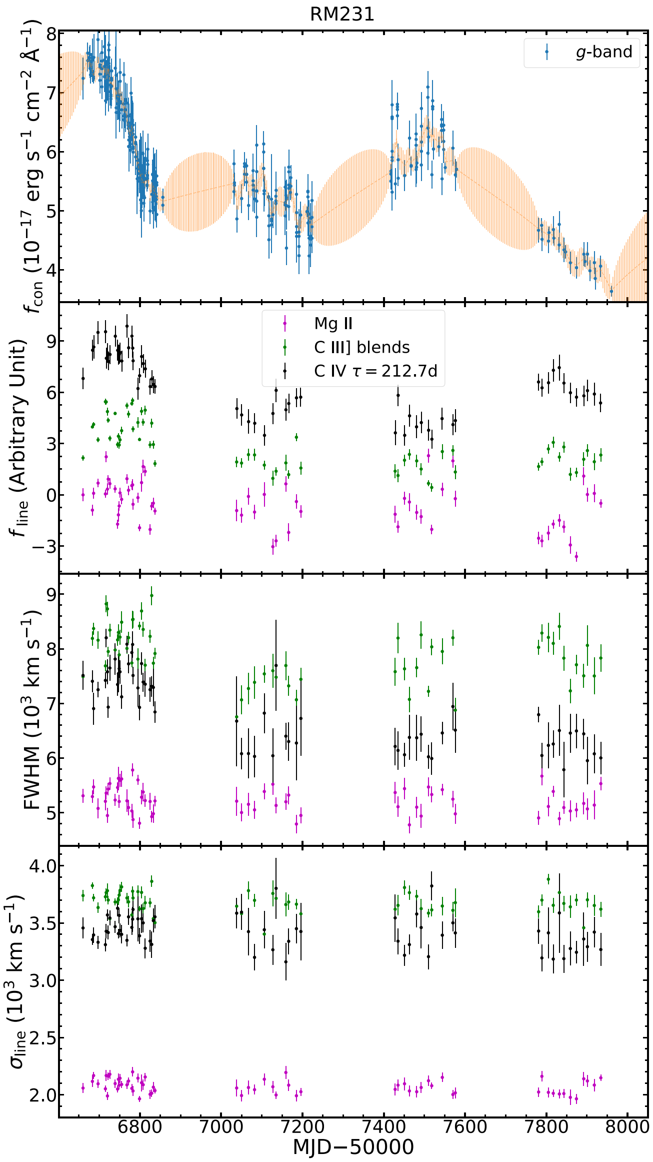

Figure 9. An example (RM231) of time variations of continuum flux $f_{\rm con}$ (first panel), line flux (second panel), line FWHM (third panel), and $\sigma_{\rm line}$ (fourth panel) of C IV, C III], and Mg II during 2014–2017. The notations are the same as Figure 5. We observe approximately anti-breathing for C IV (and less so for C III]), in particular if using FWHM, while Mg II shows no obvious response in line width.

criterion, i.e., $\mathrm{SNR}_{\rm Var,con} > 3$, in Figure 20. The sample size of the C IV Lag0 sample decreases to 10 (compared to 13 for $\mathrm{SNR}_{\rm Var,con} > 2$). For C III], there are only two objects left, which is too small to constrain the statistics. The median breathing slopes for both FWHM and $\sigma_{\rm line}$ for C IV are consistent with our fiducial results.

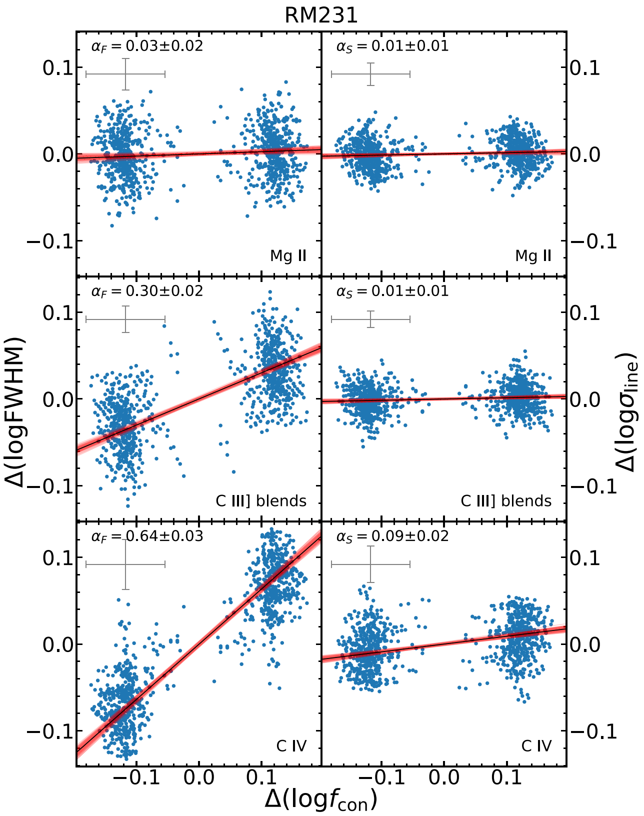

Figure 10. The $\Delta\log W - \Delta\log L$ correlation for C III] and C IV of RM231 during the 2014–2017 observations of SDSS-RM. For continuum flux $f_{\rm con}$, we use the g-band flux. C IV and the C III] blends show noticeable anti-breathing, in particular for FWHM, while Mg II is consistent with no breathing (slope close to zero). Notations are the same as Figure 6.

4. Discussion

4.1. C IV Profile Variations

The observed anti-breathing behavior for C IV is inconsistent with naive expectation from the virial relation. To understand the origin of this anti-breathing behavior, we investigate the profile variations of C IV.

We first compare the rms and mean profiles of the broad C IV line for several examples displaying clear anti-breathing in Figure 12, where the rms profile is scaled by a constant factor to best match at least one side of the wings of the line in the mean spectrum (Denney 2012). If the entire C IV line responds to continuum variations in the same way, then the scaled rms

Table 6

Breathing Effects for C III], C IV, and Si IV

		C III]				C IV				Si IV			
RMID (1)	N (2)	r_F (3)	α_F (4)	r_S (5)	α_S (6)	r_F (7)	α_F (8)	r_S (9)	α_S (10)	r_F (11)	α_F (12)	r_S (13)	α_S (14)
032	62	⋯	⋯	⋯	⋯	0.97	0.40 ± 0.01	0.90	0.19 ± 0.01	⋯	⋯	⋯	⋯
145	63	⋯	⋯	⋯	⋯	−0.66	−0.24 ± 0.04	−0.71	−0.24 ± 0.03	⋯	⋯	⋯	⋯
201	60	−0.65	−0.67 ± 0.04	−0.49	−0.08 ± 0.01	−0.70	−0.36 ± 0.02	−0.44	−0.20 ± 0.02	⋯	⋯	⋯	⋯
231	63	0.70	0.30 ± 0.02	0.10	0.01 ± 0.01	0.91	0.64 ± 0.03	0.30	0.09 ± 0.02	⋯	⋯	⋯	⋯
275	64	⋯	⋯	⋯	⋯	0.90	0.37 ± 0.01	0.77	0.14 ± 0.01	⋯	⋯	⋯	⋯
295	60	⋯	⋯	⋯	⋯	0.69	0.29 ± 0.04	0.60	0.22 ± 0.04	⋯	⋯	⋯	⋯
298	62	0.35	0.24 ± 0.05	−0.14	−0.08 ± 0.05	0.44	0.25 ± 0.05	0.19	0.22 ± 0.09	⋯	⋯	⋯	⋯
387	60	⋯	⋯	⋯	⋯	0.63	0.40 ± 0.03	0.25	0.13 ± 0.03	⋯	⋯	⋯	⋯
401	62	⋯	⋯	⋯	⋯	0.94	0.71 ± 0.01	0.92	0.24 ± 0.01	⋯	⋯	⋯	⋯
408	62	−0.06	−0.01 ± 0.10	0.15	0.11 ± 0.08	0.07	0.04 ± 0.13	0.55	0.30 ± 0.07	⋯	⋯	⋯	⋯
485	62	0.30	0.32 ± 0.13	−0.15	−0.08 ± 0.08	0.59	0.73 ± 0.13	−0.12	−0.10 ± 0.14	−0.06	0.01 ± 0.18	0.06	0.13 ± 0.14
549	63	⋯	⋯	⋯	⋯	0.25	0.07 ± 0.02	0.13	0.04 ± 0.02	⋯	⋯	⋯	⋯
827	63	⋯	⋯	⋯	⋯	0.74	0.26 ± 0.02	−0.04	−0.01 ± 0.01	⋯	⋯	⋯	⋯

Note. Same as Table 4, but for broad C III], C IV and Si IV.

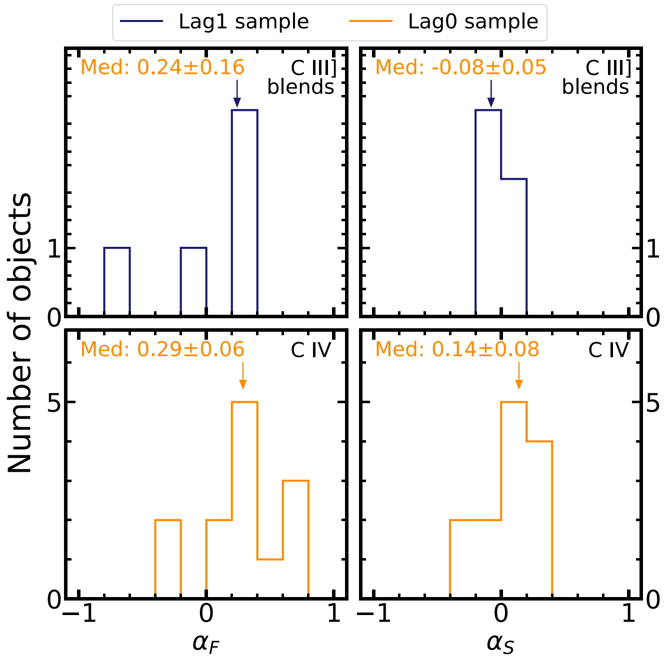

Figure 11. Distributions of the $\Delta\log W - \Delta\log L$ correlation slopes, α_F (left-hand side) and α_S (right-hand side), derived using FWHM and $\sigma_{\rm line}$, respectively, for C IV and the C III] blend.

profile should roughly match the mean profile.[22] There is a significant difference between the rms and mean C IV profiles such that the rms profile is much broader, while the mean profile likely contains an extra relatively narrower core component that is missing from the rms profile. This result is consistent with the findings in Denney (2012) on local RM AGN, where the central component does not seem to respond to continuum variations as much as the broader component during the monitoring period. As pointed out by Denney (2012), the likely origin for this central component includes a possible narrow-line region or an optically thin disk wind component (e.g., Proga et al. 2000; Proga & Kallman 2004; Waters et al. 2016) that does not respond to photoionization variability on the relevant timescales here.

It is worth noting that the peak of the C IV line in the mean spectrum is on average blueshifted by hundreds of km s^{-1} from the systemic velocity of the quasar based on low-ionization lines (Shen et al. 2016a), commonly known as the C IV blueshift (e.g., Gaskell 1982; Tytler & Fan 1992; Richards et al. 2002). This result may suggest that the non-reverberating core C IV component is more likely to be associated with a disk wind. Meanwhile, the broad-base component revealed in the rms spectrum is on average redshifted by hundreds of km s^{-1} from the systemic velocity. The latest calculations (Waters et al. 2016) of reverberation mapping signatures from photoionized disk winds based on the Proga & Kallman (2004) model reproduce many of the observed C IV properties here, such as the blueshifted non-responding line profile and the shape of the rms profile. However, the calculations in Waters et al. (2016) generally predict blueshifted rms profile from the disk wind; the observed redshifted rms profile could be explained by the so-called "hitch-hiking" gas that falls back toward the disk (T. Waters, private communications). A more thorough comparison between observed C IV line characteristics from reverberation mapping and predictions from disk wind models can further constrain the detailed structure and kinematics of the BLR.

Under this premise of two components of the broad C IV emission, where only the broader component responds to continuum variations and follows the virial relation between average BLR size and line width, we can qualitatively understand the anti-breathing behavior: when luminosity increases, the virialized broader component increases its flux and decreases its width. However, if the non-reverberating central component is significant, then the overall line width may still increase because of the enhanced flux in the wings of the line. To illustrate these effects, we perform the following idealized simulations.

We construct a simple two-component C IV model, where we use two Gaussians to describe the narrower core component and the broader base component. The core component has a fixed Gaussian width (dispersion) of 800 km s^{-1}, and the base component has an initial Gaussian width (dispersion) of 4000 km s^{-1}. The initial peak flux ratio of the two components is base: core = 1: 4. We then increase the flux of the base component to mimic the reverberation to continuum changes. For the width of the variable base component, we test two cases, where either the width varies according to the perfect breathing given by the virial relation (left-hand panel of Figure 13) or is held constant (right-hand panel of Figure 13). In both cases, we found that the change in the overall line width (core+base) component deviates significantly from the canonical breathing under the virial relation. In particular, the overall line profile always displays anti-breathing if using FWHM, and mostly no breathing (case 1) or anti-breathing (case 2) if using $\sigma_{\rm line}$, in qualitative agreement with our observations shown in Figure 11. In this simulation, there is no velocity offset between the core and base components, but the results remain the same when we offset the two components by 1500 km s^{-1} apart.

A byproduct from this two-component model for C IV is that we expect a somewhat different intrinsic (i.e., due to luminosity variations in a given object) Baldwin effect (e.g., Baldwin 1977; Kinney et al. 1990; Pogge & Peterson 1992), compared to the global (i.e., object-by-object) Baldwin effect for quasars with different luminosities. The global Baldwin effect can be reasonably well explained by a systematic change in the ionizing spectral energy distribution (SED) with quasar luminosity and the resulting photoionization response in the broad lines (e.g., Korista et al. 1998). The same photoionization effects and SED dependence should also apply to the intrinsic Baldwin effect. Additionally, because the central component largely does not respond to (or lag significantly behind) continuum changes on typical RM monitoring timescales, the intrinsic Baldwin effect is expected to have a shallower slope b in the line response to continuum changes ($L_{\rm CIV} \propto L_\lambda^b$) than the global (average) Baldwin effect, consistent with observations (e.g., Kinney et al. 1990; Pogge & Peterson 1992).

We now examine the profile changes in these C IV anti-breathing examples in detail. We use two additional parameters to characterize the shape of the C IV line: the shape parameter $S = {\rm FWHM}/\sigma_{\rm line}$ and the asymmetry parameter ${\rm Asymm} = (\lambda_{\frac{3}{4}} - \lambda_{\frac{1}{4}})/{\rm FWHM}$, where $\lambda_{\frac{1}{4}}$ and $\lambda_{\frac{3}{4}}$ are the

---

[22] A direct consequence is that the widths measured from the mean and rms spectra should correlate with each other well, as observed for the low-ionization lines Hα, Hβ and Mg II (Wang et al. 2019).

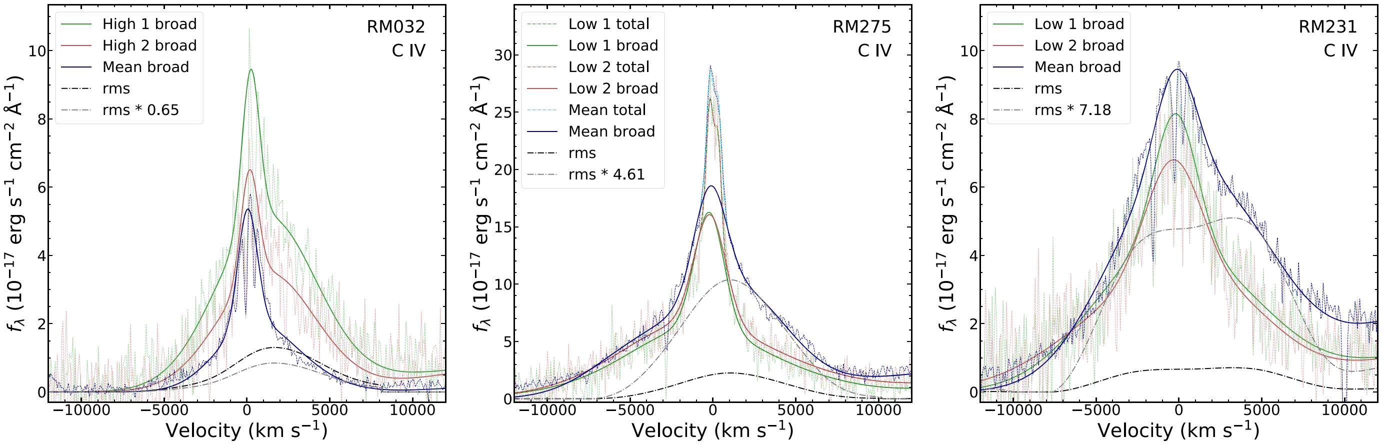

Figure 12. Broad C IV line profile variations of three examples (RMID marked in the top right-hand corner) showing anti-breathing. We show the mean (blue) and rms spectra (black dashed–dotted) of the line, as well as the profiles of two representative epochs (green and red) that show large changes in line width. We also overplot the scaled rms spectrum (gray dashed–dotted) that matches at least one side of the mean profile (see text for details). The narrow core of the mean broad-line profile is generally missing from the rms profile.

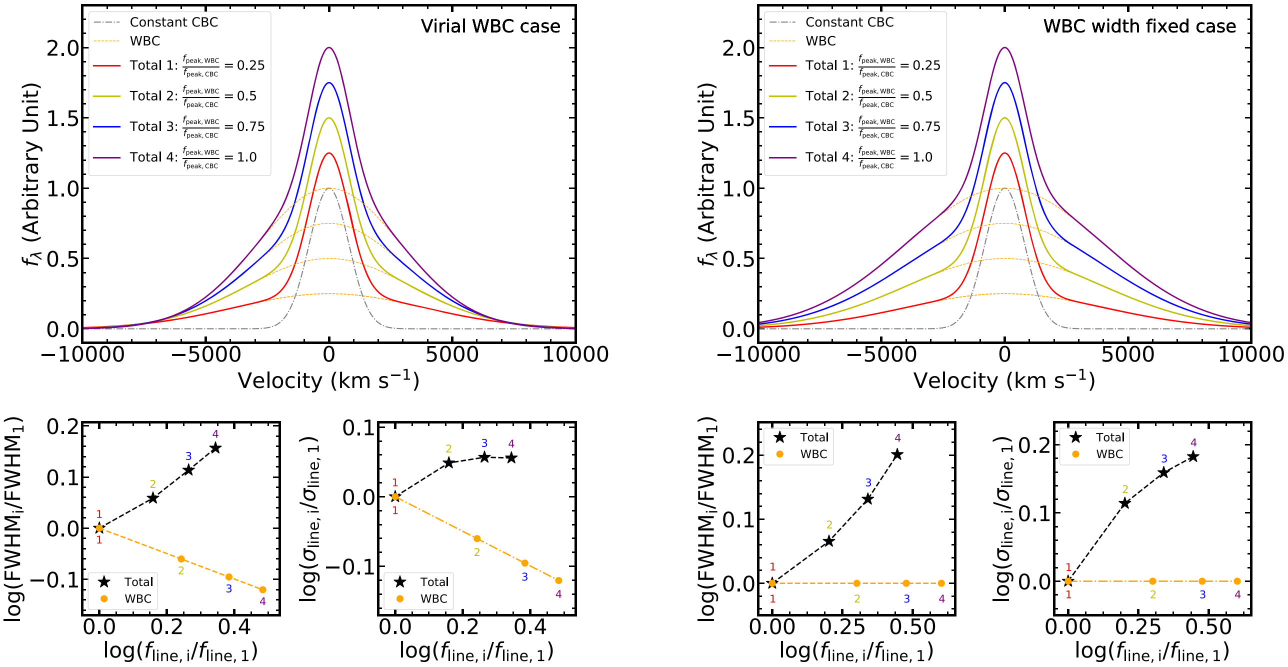

Figure 13. Idealized simulations of the two-components model, a Core Broad Component (CBC) that is non-reverberating and a Wing Broad Component (WBC) that may or may not be reverberating, of C IV profile (top) and the $\Delta \log W - \Delta \log L$ relations (bottom). We test two cases: (1) the WBC follows the expected canonical breathing (left-hand side) and (2) the WBC width remains constant (right-hand side). In both cases, the CBC (gray) has fixed width and flux, while the WBC (orange) varies in flux. When we increase the flux in the WBC as indicated by the numbers 1–4, we find that the line width of the "total" profile (CBC + WBC) displays an anti-breathing effect, as observed.

wavelengths at $\frac{1}{4}$ and $\frac{3}{4}$ of the peak line flux, respectively. We found that when the continuum flux increases in the anti-breathing examples shown in Figure 12, the flux in the line wings increases more than in the core. This is consistent with our earlier findings that most of the line variability is contained in the broader base component and the narrower core component shows less variability. If the broader component has a velocity offset from the core component, then increasing its flux will also increase the line asymmetry. The fact that the shape parameter S changes as flux changes also confirms that the narrow core of C IV does not reverberate in the same way as the broader component. However, we do not believe that we are observing velocity-resolved reverberation of C IV because the rms line profile computed over the entire 4 yr monitoring period generally lacks a narrow core rms component.

The existence of a non-varying core component in C IV will lead to enhanced scatter between the line widths measured from the mean and rms spectra. In Figure 14, we compare the correlations between the mean and rms line widths for different lines. The correlations are indeed worse for C IV than for the low-ionization broad lines studied in Wang et al. (2019). The correlation is particularly poor when we use FWHM. For $\sigma_{\rm line}$,

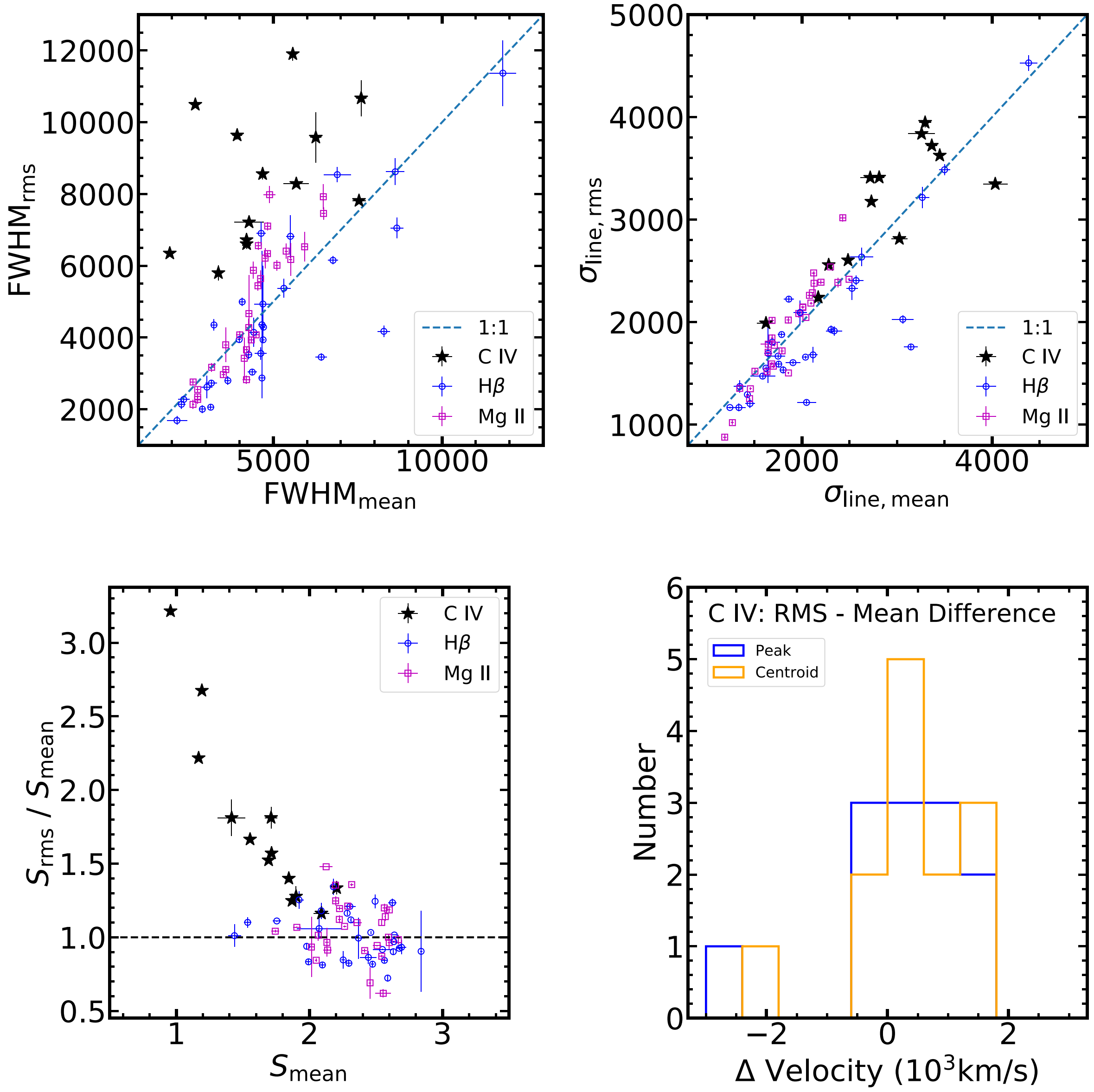

Figure 14. Rms and mean profile comparisons for Hβ, Mg II, and C IV. The upper two panels are comparisons for FWHM and $\sigma_{\rm line}$, respectively. The lower two panels are line shape ratio comparison and centroid velocity difference distribution, respectively. C IV shows noticeable worse correlation between the rms and mean widths than Hβ and Mg II, which is mainly due to the non-reverberating core component (see text for details). This non-varying core C IV component has less impact on $\sigma_{\rm line}$ than on FWHM.

the correlation between the mean and rms widths for C IV is reasonably good because the variable line wings contribute significantly to the $\sigma_{\rm line}$ measurements.

The idea of a two-component model for the C IV line is not new. Wills et al. (1993) performed a principal components analysis on a sample of 15 quasars and found a negative correlation between C IV EW and FWHM in a statistical sense. Considering the C IV Baldwin effect (Baldwin 1977), this means that there is a positive correlation between continuum luminosity and C IV FWHM. This is similar to the anti-breathing effect discussed here. Wills et al. (1993) proposed a two-component model for C IV, where they attributed the core component to the emission from an intermediate line region (ILR, also see Brotherton et al. 1994) that is the inner extension of the narrow-line region. Variants of the ILR argument and extension to low-ionization lines are further explored in Hu et al. (2008a, 2008b) and Hu et al. (2012). More recently, Denney (2012) revisited this idea by showing that there is a central non-reverberating part of C IV in local RM AGN, which is similar to our findings here. Denney (2012) subtracted the scaled rms profile from the mean profile and found that the central component often has a blue asymmetry, which is roughly anti-correlated with the EW of the central component. Denney (2012) argued that this central component could be orientation dependent (face-on objects show more blue asymmetry and less peak value), from either an optically thin (non-reverberating) BLR outflow, or the ILR (much longer time to reverberate). The association of the non-reverberating central component to BLR outflows such as a disk wind is further reasoned in Richards et al. (2011, and references therein). Our results for high-redshift quasars with C IV RM data are consistent with these earlier studies, and generally support the two-component model for C IV.

The average C IV peak blueshift in the mean profile is observed to increase with quasar luminosity over a population of quasars

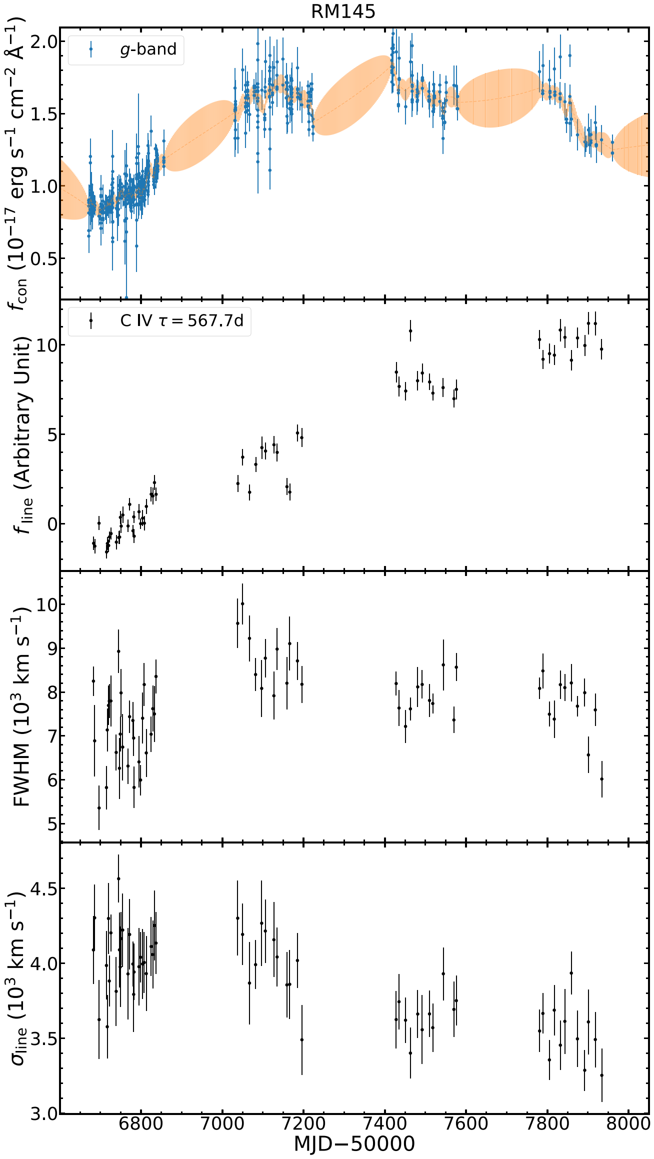

Figure 15. Same as Figure 5 but of RM145, which shows overall normal breathing for C IV during the four-year monitoring of SDSS-RM.

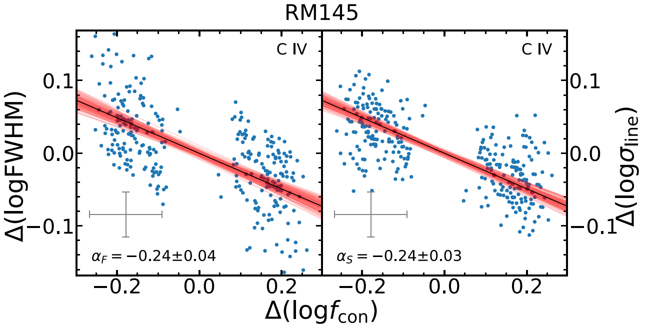

Figure 16. Same as Figure 10 but for RM145, which shows normal breathing for C IV. Notations are the same as Figure 6.

(e.g., Richards et al. 2011; Shen et al. 2016a), and can well reach more than 1000 km s^{-1} in the most luminous quasars. If we ascribe the non-reverberating core component to a disk wind, then the relative contribution of this wind component depends on the luminosity (and mostly likely, the Eddington ratio $L/L_{\rm Edd}$ as well) of the quasar. However, for individual objects, the variability of this core component and its blueshift is mild or undetectable within typical monitoring durations of less than a few years, consistent with the findings in e.g., Sun et al. (2018). Thus the large dynamic range in C IV blueshift observed over the population of quasars must be driven on much longer timescales, when the long-term-average luminosity state is substantially maintained to establish a new dynamical equilibrium of the wind. Qualitatively, the global dependence of the relative contribution of the non-reverberating component can explain the difference between single-epoch BH masses and RM-based masses as a function of $L/L_{\rm Edd}$ or simply L. Although fully understanding the physical mechanisms of this wind component is beyond the scope of this work, it is worth exploring in future theoretical studies of disk winds in quasars.

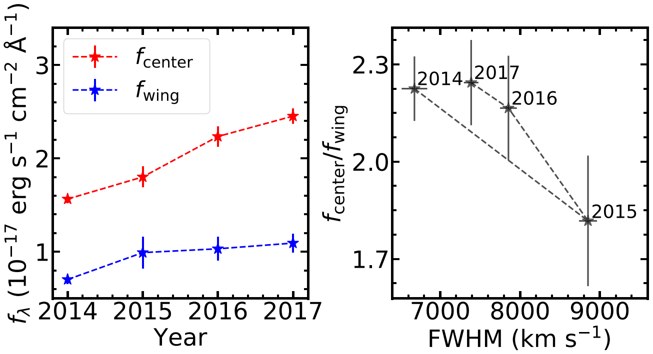

Figure 17. Flux variations of the core (estimated at $v = 0$ km s^{-1}) and the wing (estimated at $v = 5000$ km s^{-1}) of the broad C IV profile of RM145 during 2014–2017.

We conclude this section by noting that some quasars still show normal breathing in C IV, which is expected if the reverberating component dominates the C IV line (e.g., Richards et al. 2011). In our sample, RM201 and RM145 are two examples showing normal breathing. RM145 is a particularly interesting object. As can been seen in Figures 15 and 16, this object showed normal breathing overall in the four-year monitoring. However, it actually showed anti-breathing from the first to the second seasons and it then went back to normal breathing in the remaining seasons, as shown in Figure 17. The changes in breathing slope are more obvious for FWHM. We also examined the red-wing asymmetry. We use the flux at $v = 5000$ km s^{-1} for the red wing, and the flux at $v = 0$ km s^{-1} for the core. As shown in Figure 17, the core and wing fluxes both increased during the four-year monitoring. However, the core to red-wing flux ratio decreased in the first two years and it then increased in the following years. Since the continuum flux largely monotonically increased during the first three years of monitoring, this transition could result from the lagged response of the core component than the wing component. This could be evidence that the core component is located further away but still reverberates to continuum changes.

4.2. C III] and Si IV Breathing

In our high-z sample, we have five quasars for which we can measure the breathing effect for the C III]+Al III+Si III] complex. As shown in Figure 11 and Table 6, C III] displays similar breathing behaviors as C IV, with most objects showing an anti-breathing. At first glance this may appear to be unexpected because C III] has a lower ionization potential than C IV. However, the width of C III] is shown to correlate with the C IV width (e.g., Shen & Liu 2012). Our finding of similar C III]

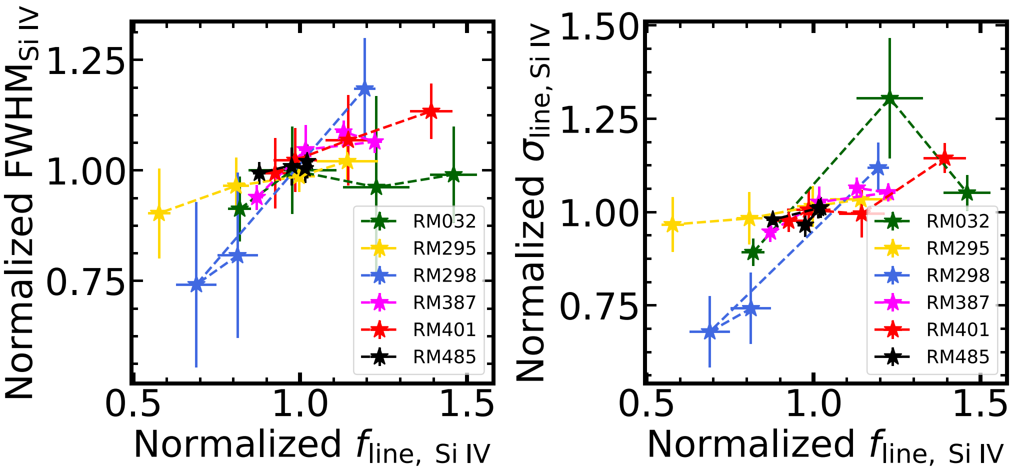

Figure 18. Correlations between line widths and line flux for Si IV, measured from seasonally coadded spectra for six quasars in our sample. The overall positive correlations suggest that Si IV displays an anti-breathing effect, similar to C IV.

and C IV breathing is consistent with the scenario where C IV and C III] emission originates from similar regions.

There is only one quasar that passes our S/N criteria for studying Si IV breathing. To boost the S/N of spectral measurements, we use the yearly coadded spectra on Si IV. There are six quasars for which we can robustly measure Si IV widths in at least two yearly coadded spectra. We plot the Si IV FWHM–$f_{\rm line}$ and $\sigma_{\rm line}$–$f_{\rm line}$ relations in Figure 18. Both line widths increase with line flux, suggesting anti-breathing for Si IV. The C IV line shows similar anti-breathing in these quasars.

4.3. Implications on BLR Structure and Single-epoch BH Masses

The breathing behaviors for different broad lines suggest different structures and likely also different emission mechanism of these lines. While Hβ most closely follows the expected normal breathing under the virial assumption, the two other lines with similar ionizing potentials (Hα and Mg II) show less breathing. In particular, Mg II displays almost no breathing, along with less response in flux to continuum changes than the Balmer lines, which is consistent with earlier results (e.g., Shen 2013; Yang et al. 2020). Guo et al. (2020) performed photoionization calculations of the three low-ionization lines and were able to qualitatively reproduce their different breathing behaviors given that the Mg II and Hα emitting gas is located further out than the Hβ emitting gas. In particular, if most of the Mg II-emitting gas is near the physical boundary of the BLR, which changes on much longer dynamical timescales, then changes in luminosity will not significantly change the average distance of Mg II-emitting gas, leading to mostly no breathing.

Meanwhile, C IV mostly displays an anti-breathing. The fact that the width of C IV does change as luminosity changes suggests that at least part of the C IV-emitting gas is responding to continuum variations. Section 4.1 further demonstrated that this anti-breathing can be explained if C IV also contains a non-reverberating core component.

These different breathing behaviors have direct consequences on the single-epoch BH masses (e.g., Shen 2013) that rely on line widths measured from single-epoch spectroscopy. Any deviations from the expected breathing slope of $\alpha = -0.25$ would introduce a luminosity-dependent bias in the single-epoch BH mass (e.g., Shen & Kelly 2010; Shen 2013). While this extra mass bias due to intrinsic quasar variability is still well within the envelope of the systematic uncertainty (~0.4 dex) of virial BH mass estimates, given typical amplitude of quasar variability, it may become important when studying flux-limited statistical quasar samples (see detailed discussions in Shen 2013). Another situation where the lack of breathing may be important is for extreme variability quasars (EVQs) that can vary by more than one magnitude over multi-year timescales (e.g., Rumbaugh et al. 2018). Repeated spectroscopy for these EVQs shows that the Mg II width remains more or less constant when continuum luminosity varies substantially (e.g., Yang et al. 2020), resulting in significant luminosity-dependent bias in the single-epoch masses.

In all of the cases that we studied, it appears that the line dispersion $\sigma_{\rm line}$ measured from single-epoch spectra more closely follows the expected virial relation than FWHM; however, deviations still exist, even with $\sigma_{\rm line}$. This offers support to use $\sigma_{\rm line}$ as a more reliable indicator for the virial velocity in single-epoch spectroscopy, provided that this quantity can be robustly measured. Wang et al. (2019) provided an empirical recipe to measure $\sigma_{\rm line}$ robustly.

Based on the breathing results, we therefore conclude that Hβ (and to a lesser extent, Hα) remains the most reliable line to use as a single-epoch virial mass estimator. Mg II is not as reliable as Hβ, given the general behavior of no breathing. C IV is the least reliable line to use as a single-epoch virial mass estimator, given the anti-breathing behavior; however, using $\sigma_{\rm line}$ can mitigate the situation to some extent.

Our analysis does not address the question of whether or not the measured line widths from single-epoch spectra provide reasonable estimates of the average virial velocity for a global population of quasars with different BH masses and luminosities. The breathing effects studied here only provide the extra scatter in single-epoch mass estimates due to intrinsic quasar variability. Following Equation (2), the deviation in the single-epoch BH mass estimate for a given quasar scales with the luminosity deviation as $\delta \log M_{\rm BH} = (2\alpha + 0.5)\delta \log L$. Therefore for typical quasar rms variability of 0.1 dex and $\alpha = 0$ (no breathing), the intrinsic variability-induced scatter in the single-epoch BH mass estimate is only 0.05 dex. However, for extreme quasar variability (more than one magnitude variations, e.g., Rumbaugh et al. 2018) and an anti-breathing slope of $\alpha = 0.25$ (using C IV FWHM), the intrinsic variability-induced scatter is 0.4 dex.

5. Summary

In this work we have studied the breathing effect (i.e., the changes in broad line width in response to flux variations) for various broad lines using photometric and spectroscopic monitoring data from the SDSS-RM project. Our final sample includes 21 Hα, 31 Hβ, 26 Mg II, 5 C III], 13 C IV and 1 Si IV quasars for which we can reliably measure breathing; these quasars cover a wide redshift range ($z \approx 0.1$–2.5). While there have been similar studies on a few individual low-z RM AGN focusing on the broad Hβ line (e.g., Park et al. 2012), or using few-epoch repeated spectroscopy for large quasar samples (e.g., Wilhite et al. 2006; Shen 2013), our work is the first comprehensive study on the breathing effect with RM monitoring data for statistical quasar samples and for most of the major quasar broad emission lines. Confirming and extending the earlier results, our main findings are as follows:

1. When the lag between line response and continuum variations is taken into account, broad Hβ mainly shows normal breathing (i.e., line width decreases as luminosity increases), and the slope of the breathing is most consistent with the expectation from the virial relation. Meanwhile, broad Hα on average shows much less breathing. The delay in the line responses to continuum variations will tend to further flatten the breathing slope if both the continuum luminosity and line width are measured from the same epoch.
2. Broad Mg II on average shows no breathing (i.e., the line width responds less to luminosity changes than broad Hβ), which is consistent with earlier results (Shen 2013; Yang et al. 2020). This result can be qualitatively understood by the possibility that the Mg II-emitting gas is near the physical boundary of the BLR, and thus will not expand or contract freely when luminosity changes (e.g., Guo et al. 2020).
3. Importantly, the broad C IV line mostly shows an anti-breathing mode; that is, line width increases with luminosity, consistent with earlier findings based on non-RM data (e.g., Wills et al. 1993; Wilhite et al. 2006; Shen 2013). This anti-breathing can be explained by a two-component model for broad C IV emission, a broad-base reverberating component, and a narrower (but still broader than typical narrow lines), core component that does not respond to luminosity variations as strongly as the reverberating component. This is consistent with the findings in e.g., Denney (2012) based on local RM results, and follows the general idea of two components for the C IV emission (e.g., Wills et al. 1993; Richards et al. 2011). However, the nature of this non-reverberating component remains unclear. It could originate from either an Intermediate Line Region (ILR, e.g., Wills et al. 1993; Brotherton et al. 1994) or from a disk wind (e.g., Proga et al. 2000; Proga & Kallman 2004; Waters et al. 2016). The existence of a non-reverberating broad C IV component underlies the large scatter between the broad C IV widths measured from the mean and rms spectra, and the long-argued caveats in single-epoch BH masses based on C IV (e.g., Baskin & Laor 2005; Sulentic et al. 2007; Shen et al. 2008; Shen & Liu 2012; Coatman et al. 2017).
4. Despite these average behaviors, individual objects can show normal breathing in any of the broad lines studied here.
5. These diverse breathing behaviors suggest additional uncertainty due to intrinsic quasar variability in the single-epoch virial BH mass estimates that rely on the line width measured from single-epoch spectroscopy. In particular, any deviation from the expected breathing from a perfect virial relation would lead to a luminosity-dependent bias (e.g., Shen & Kelly 2010; Shen 2013) in the single-epoch mass estimate. Based on the observed breathing behaviors, C IV (and C III], Si IV to some extent as well) would have the largest extra scatter due to quasar variability for single-epoch BH mass estimates. Mg II and Hα will also induce extra scatter in single-epoch masses because of quasar variability, given their deviations from the expected breathing behavior from the virial relation.
6. We find evidence for Hβ that $\sigma_{\rm line}$ could be better than FWHM in preserving the normal breathing behavior, although significant deviations are still present in most cases.

The different breathing behaviors are generally consistent with earlier photoionization models (e.g., Goad et al. 1993; Guo et al. 2020) and qualitative ideas put forward for the C IV BLR (e.g., Wills et al. 1993; Richards et al. 2011; Denney 2012). These breathing observations provide valuable information to constrain the different distributions of line-emitting gas and the kinematic structures of the BLR for different line species in future modeling of the BLR.

The extra scatter in single-epoch BH mass estimates due to quasar variability scales with the scatter in luminosity as $\delta \log M_{\rm BH} = (2\alpha + 0.5)\delta \log L$. This is generally negligible compared with the ~0.4 dex uncertainty in single-epoch mass estimates. However, for lines with anti-breathing (in particular C IV) and for large-amplitude quasar variability, this luminosity-dependent bias[23] in single-epoch mass estimate becomes important. Rumbaugh et al. (2018) has showed that if selection effects are accounted for, then quasar variability exceeding one magnitude is not uncommon over multi-year timescales. Thus, this luminosity-dependent bias due to abnormal breathing is particularly relevant when using flux-limited quasar samples with single-epoch mass estimates to measure the distribution of BH masses and Eddington ratios (e.g., Shen & Kelly 2010, 2012). Our work highlights the importance of obtaining direct RM-based BH masses to mitigate the uncertainties in single-epoch BH masses, especially for those based on the C IV line.

We acknowledge support from the National Science Foundation of China (11721303, 11890693, 11991052) and the National Key R&D Program of China (2016YFA0400702, 2016YFA0400703). Y.S. acknowledges support from an Alfred P. Sloan Research Fellowship and NSF grant AST-1715579. C.J.G., W.N.B., J.R.T., and D.P.S. acknowledge support from NSF grants AST-1517113 and AST-1516784. K.

---

[23] In addition to abnormal breathing, there could be other factors that will lead to similar luminosity-dependent biases in single-epoch BH mass estimates, such as intrinsic scatter in the BLR $R - L$ relation. We recommend the reader to Shen (2013) for a comprehensive discussion on the systematic biases in single-epoch BH masses.

H. acknowledges support from STFC grant ST/R000824/1. P. B.H. acknowledges support from NSERC grant 2017-05983. Y.H. acknowledges support from NASA grant HST-GO-15650. We thank Tim Waters and Daniel Proga for useful discussion and the anonymous referee for suggestions that have improved the manuscript.

This work is based on observations obtained with MegaPrime/MegaCam, which is a joint project of CFHT and CEA/DAPNIA, at the Canada–France–Hawaii Telescope (CFHT) that is operated by the National Research Council (NRC) of Canada, the Institut National des Sciences de l'Univers of the Centre National de la Recherche Scientifique of France, and the University of Hawaii. The authors recognize the cultural importance of the summit of Maunakea to a broad cross section of the Native Hawaiian community. The astronomical community is most fortunate to have the opportunity to conduct observations from this mountain.

Funding for the Sloan Digital Sky Survey IV has been provided by the Alfred P. Sloan Foundation, the U.S. Department of Energy Office of Science, and the Participating Institutions. SDSS-IV acknowledges support and resources from the Center for High-Performance Computing at the University of Utah. The SDSS website is www.sdss.org. SDSS-IV is managed by the Astrophysical Research Consortium for the Participating Institutions of the SDSS Collaboration including the Brazilian Participation Group, the Carnegie Institution for Science, Carnegie Mellon University, the Chilean Participation Group, the French Participation Group, Harvard-Smithsonian Center for Astrophysics, Instituto de Astrofísica de Canarias, The Johns Hopkins University, Kavli Institute for the Physics and Mathematics of the Universe (IPMU)/University of Tokyo, the Korean Participation Group, Lawrence Berkeley National Laboratory, Leibniz Institut für Astrophysik Potsdam (AIP), Max-Planck-Institut für Astronomie (MPIA Heidelberg), Max-Planck-Institut für Astrophysik (MPA Garching), Max-Planck-Institut für Extraterrestrische Physik (MPE), National Astronomical Observatories of China, New Mexico State University, New York University, University of Notre Dame, Observatário Nacional/MCTI, The Ohio State University, Pennsylvania State University, Shanghai Astronomical Observatory, United Kingdom Participation Group, Universidad Nacional Autónoma de México, University of Arizona, University of Colorado Boulder, University of Oxford, University of Portsmouth, University of Utah, University of Virginia, University of Washington, University of Wisconsin, Vanderbilt University, and Yale University.

Facilities: Sloan, CFHT, Bok.

Appendix A
Tests on More Stringent Sample Cuts

We provide the distributions of breathing slopes for samples defined by a more stringent continuum S/N cut, $\mathrm{SNR}_{\mathrm{Var,con}} > 3$, in Figures 19 and 20.

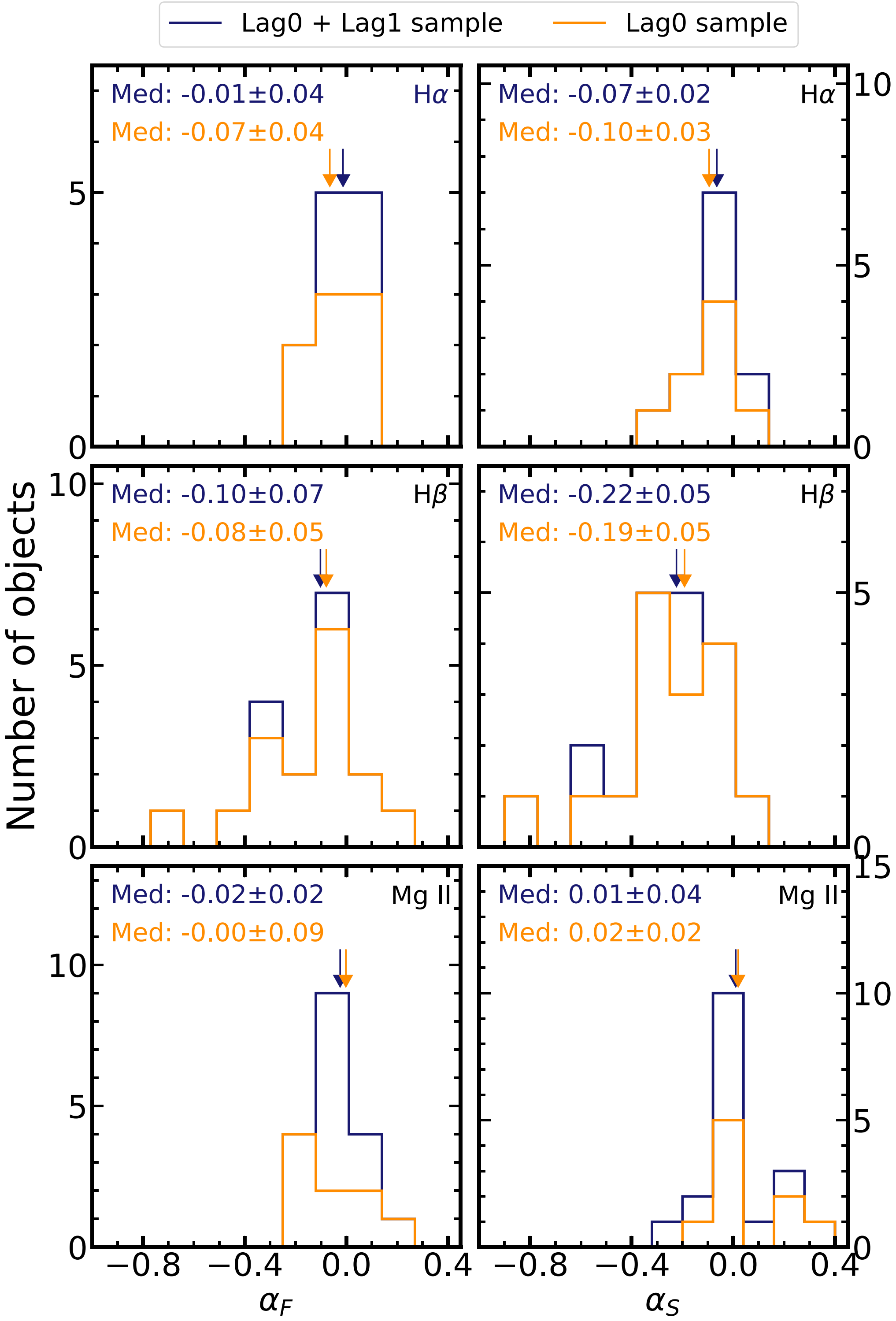

Figure 19. Same as Figure 8 but for the sample of $\mathrm{SNR}_{\mathrm{Var,con}} > 3$. The median slopes of H$\alpha$, H$\beta$, and Mg II results are generally consistent with those in Figure 8.

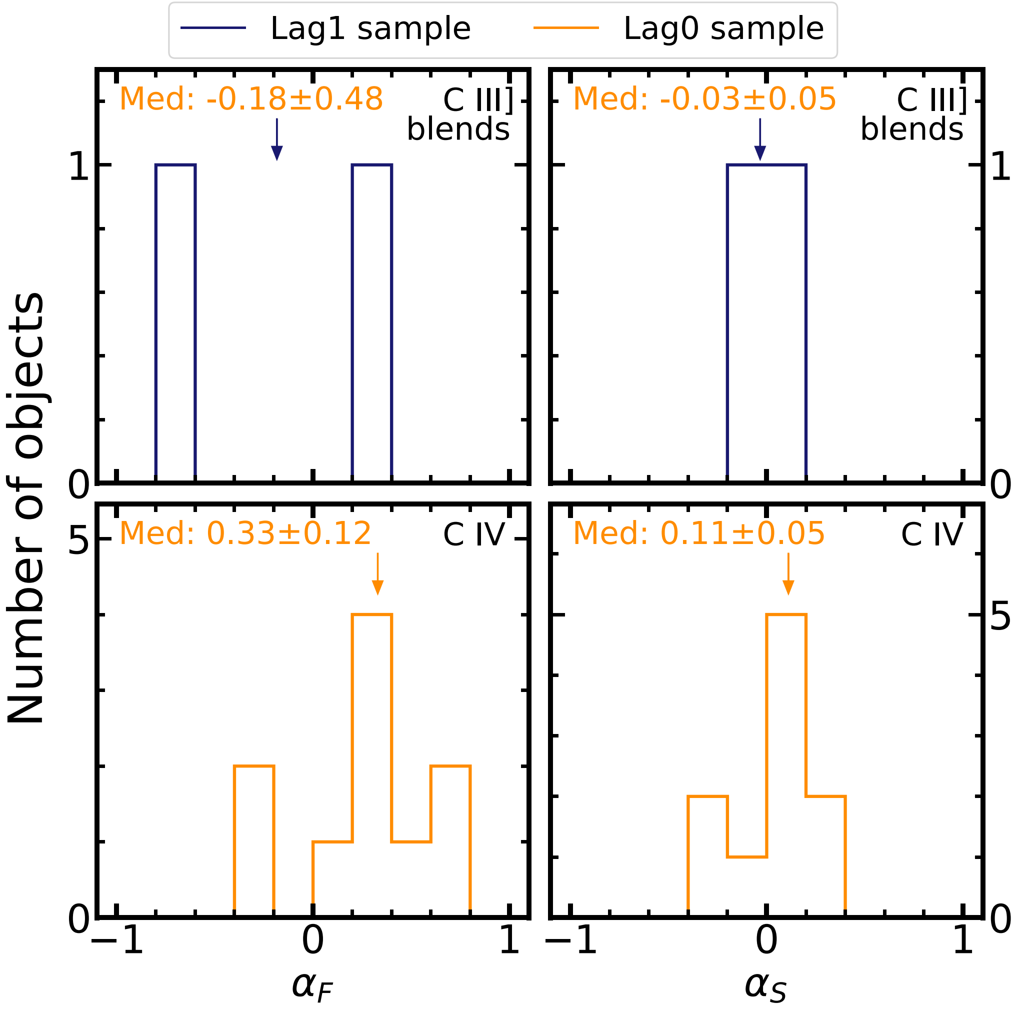

Figure 20. Same as Figure 11 but for the sample of $\mathrm{SNR_{Var,con}} > 3$. For C III], there are only two objects left and it is difficult to constrain the statistics. For C IV, the results are consistent with those in Figure 11.

Appendix B
Mean and rms Line Profiles

We provide the mean and rms line profiles for all of the objects in our final sample in Figures 21–26. Figure notations are the same as Figure 12. For clarity, we only show the model profiles. The mean profiles are from our spectral fits described in Section 3.2 and the rms profiles are from PrepSpec output. The scaled rms profiles are derived by matching the line flux between the rms model and the mean model in the window of $[-2.5 \times \mathrm{MAD_{mean}}, 2.5 \times \mathrm{MAD_{mean}}]$.

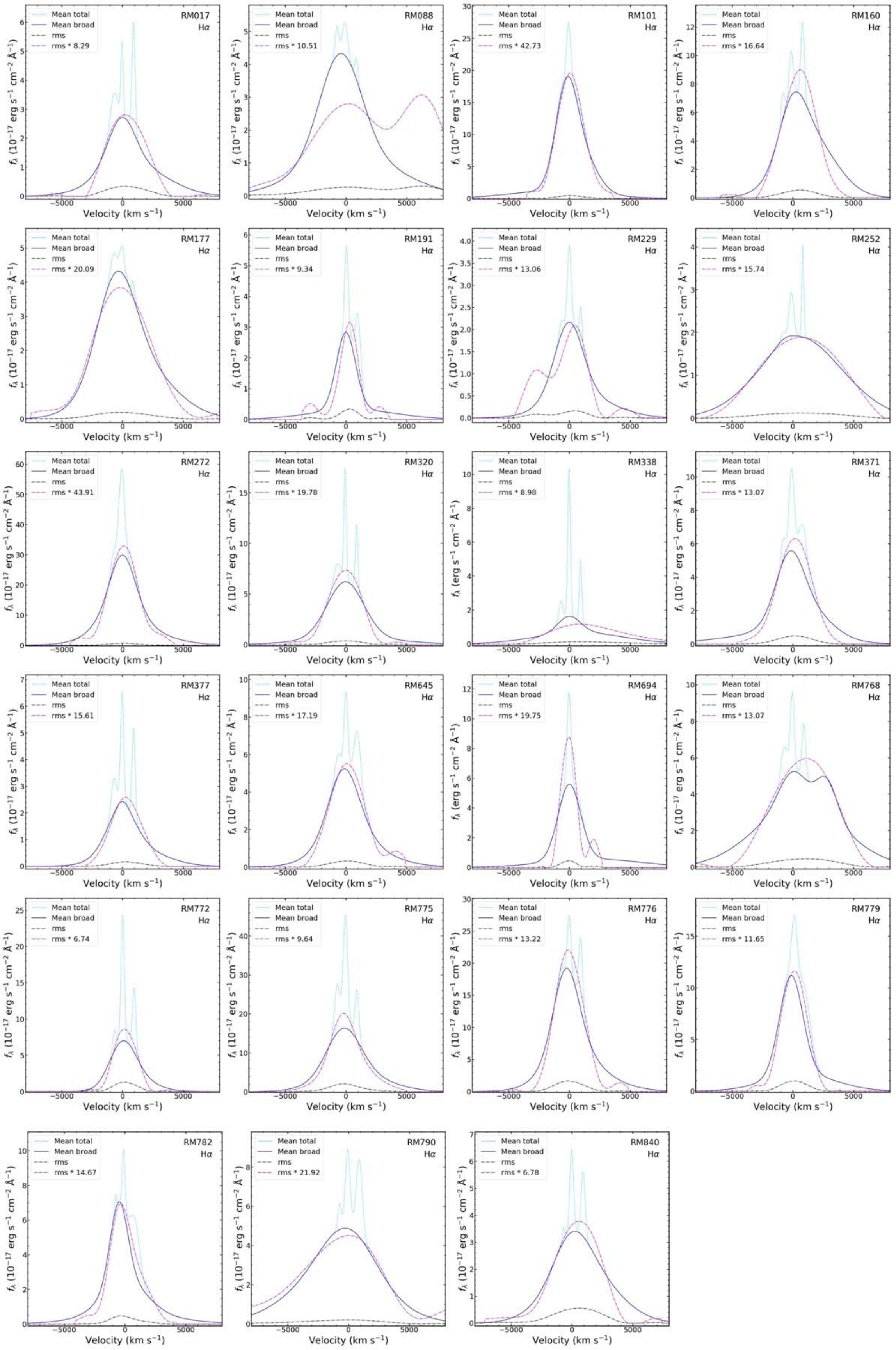

Figure 21. Mean and rms profiles of Hα. For clarity, we only show the model profiles. The mean profiles are from our spectral fits described in Section 3.2, and the rms profiles are output by PrepSpec. We also plot a scaled rms profile that matches the integrated flux of the mean broad profile within the window of $\sigma_{\rm line}$ calculation (Section 3.2).

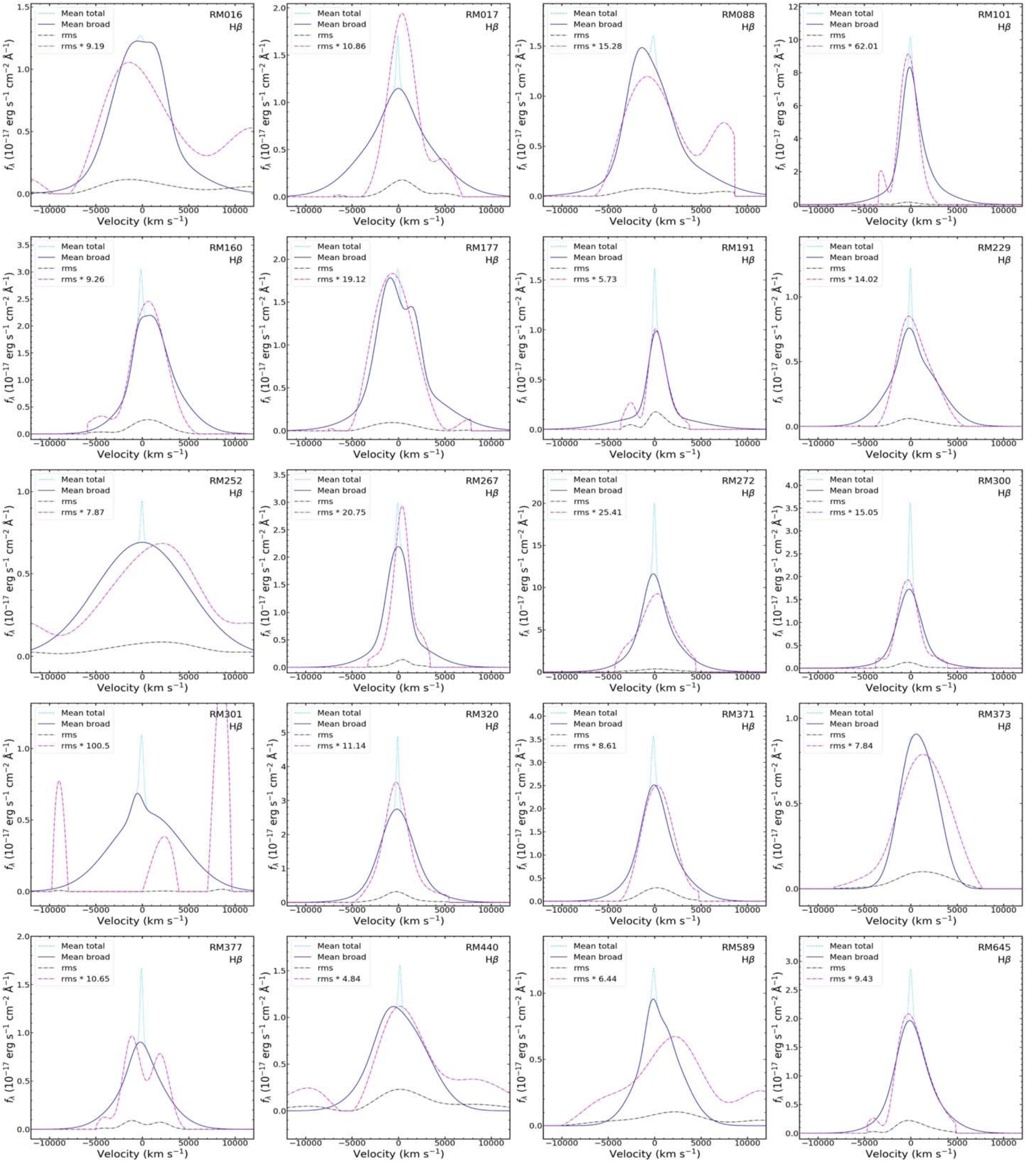

Figure 22. Same as Figure 21 but for Hβ. PrepSpec failed to produce the correct rms profile for RM301 based on the first-season data.

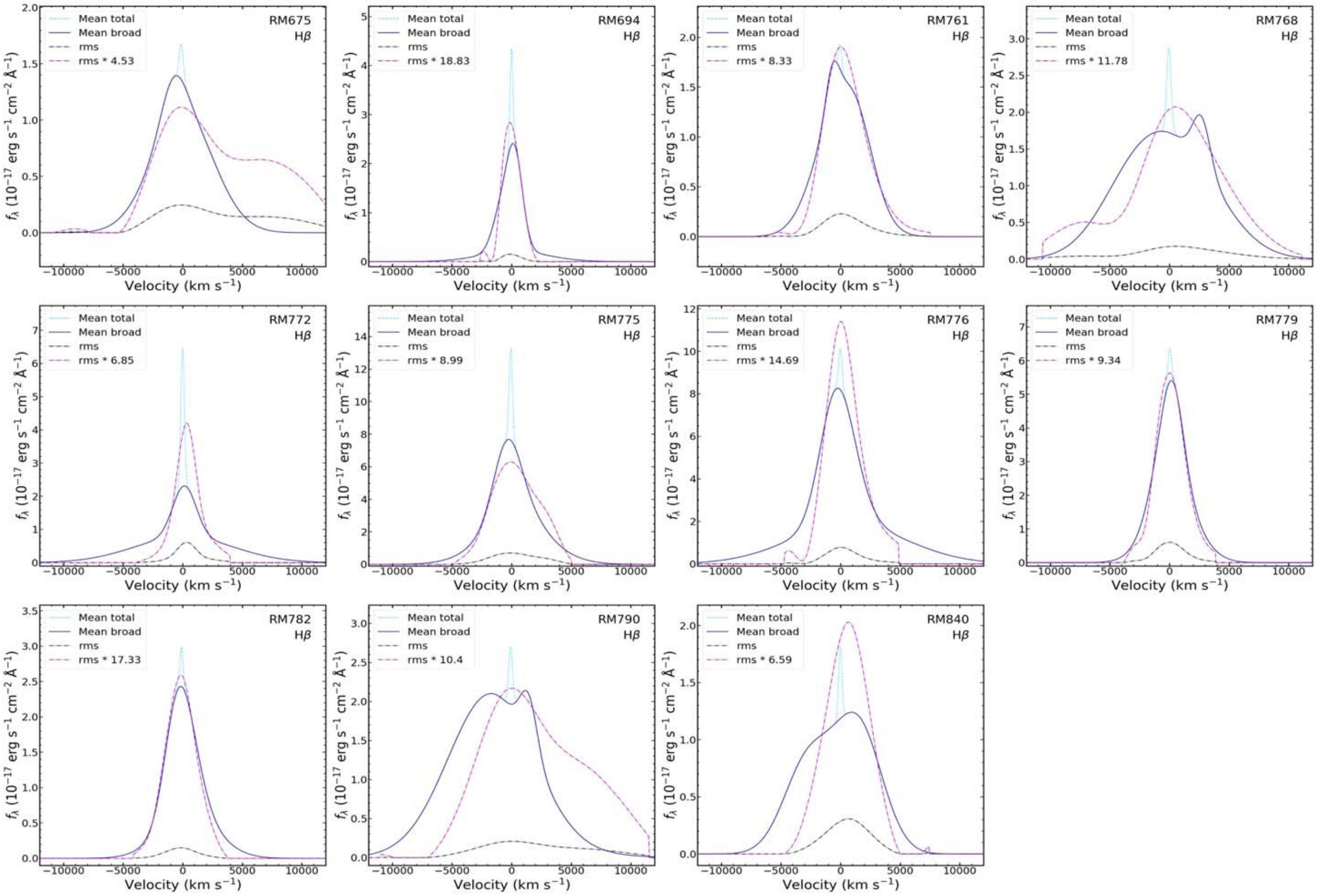

Figure 22. (Continued.)

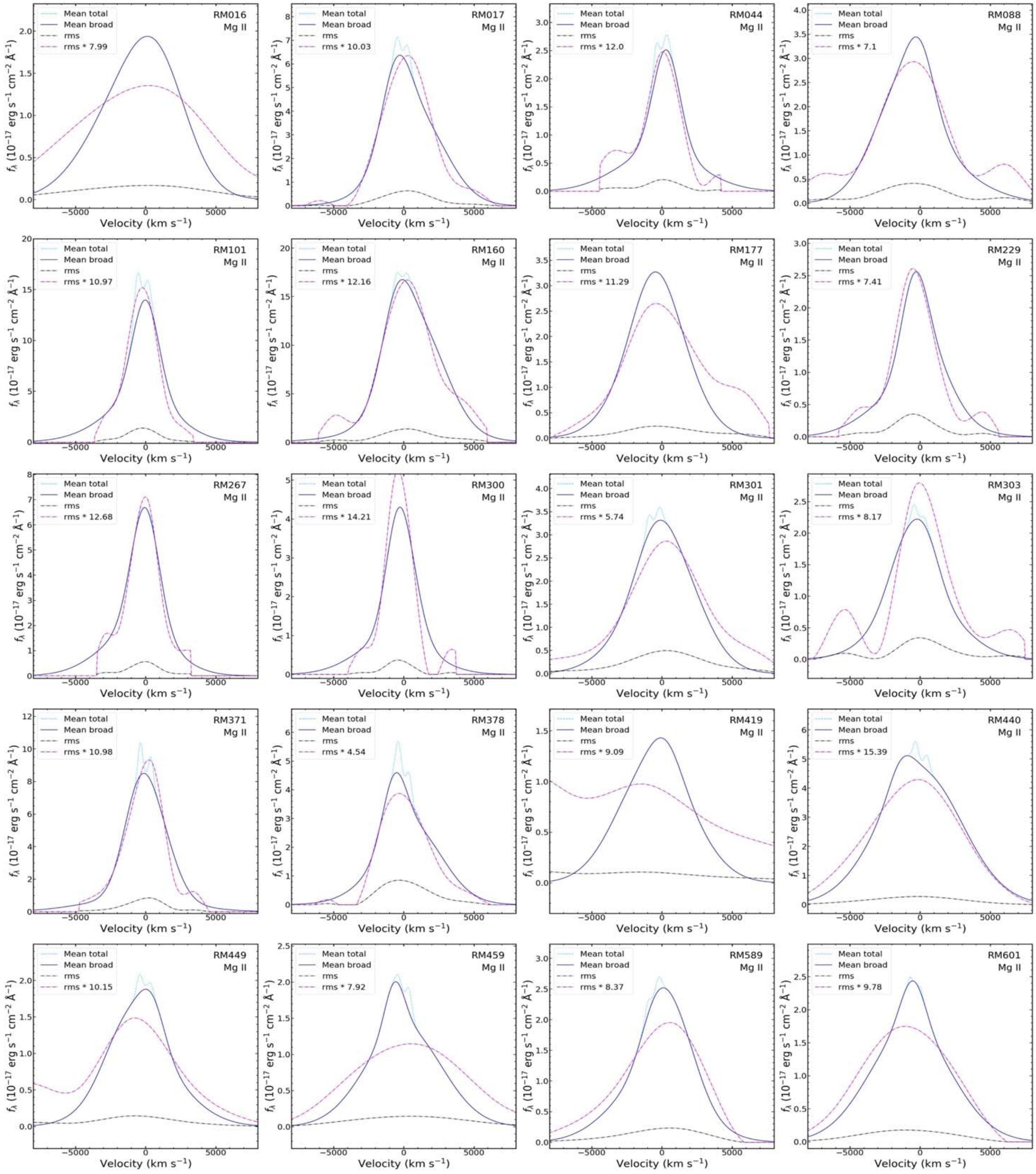

Figure 23. Same as Figure 21 but for Mg II.

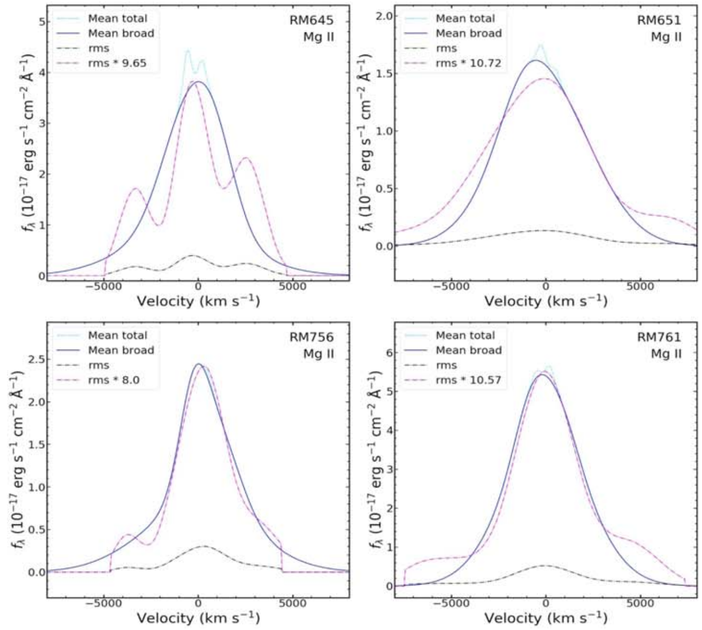

Figure 23. (Continued.)

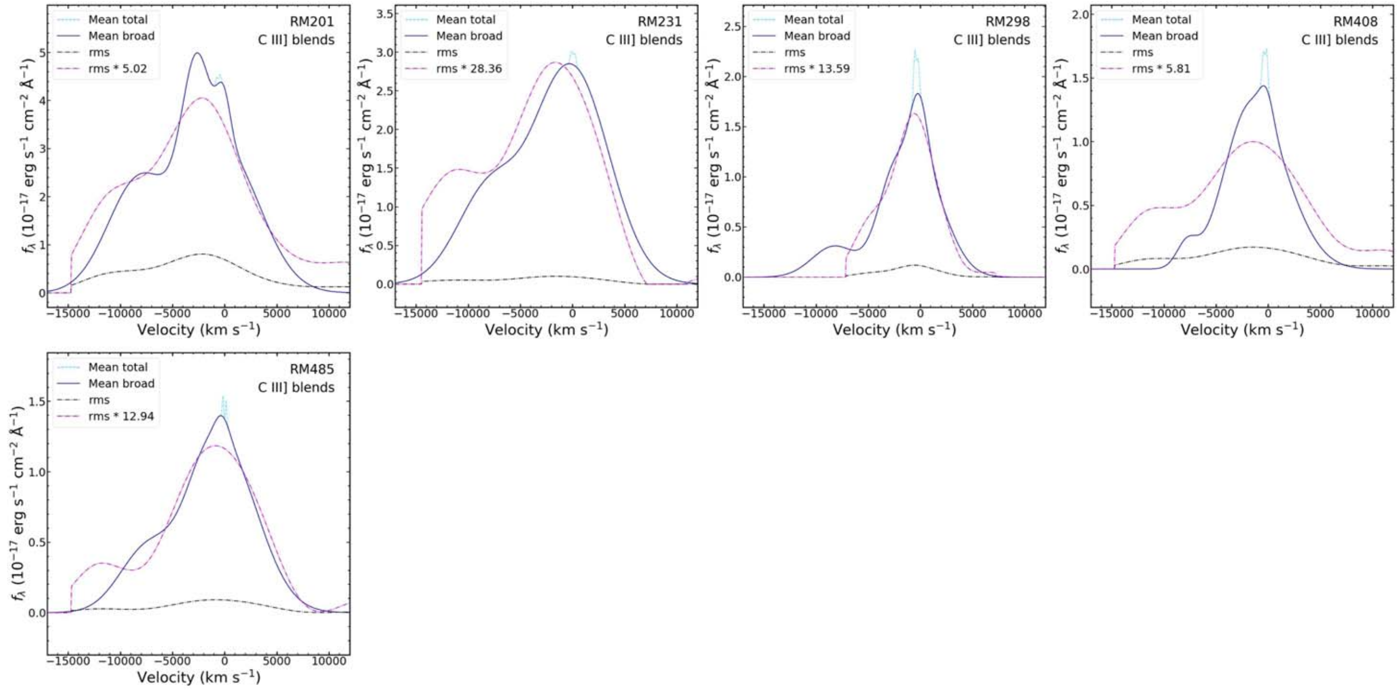

Figure 24. Same as Figure 21 but for C III] blends.

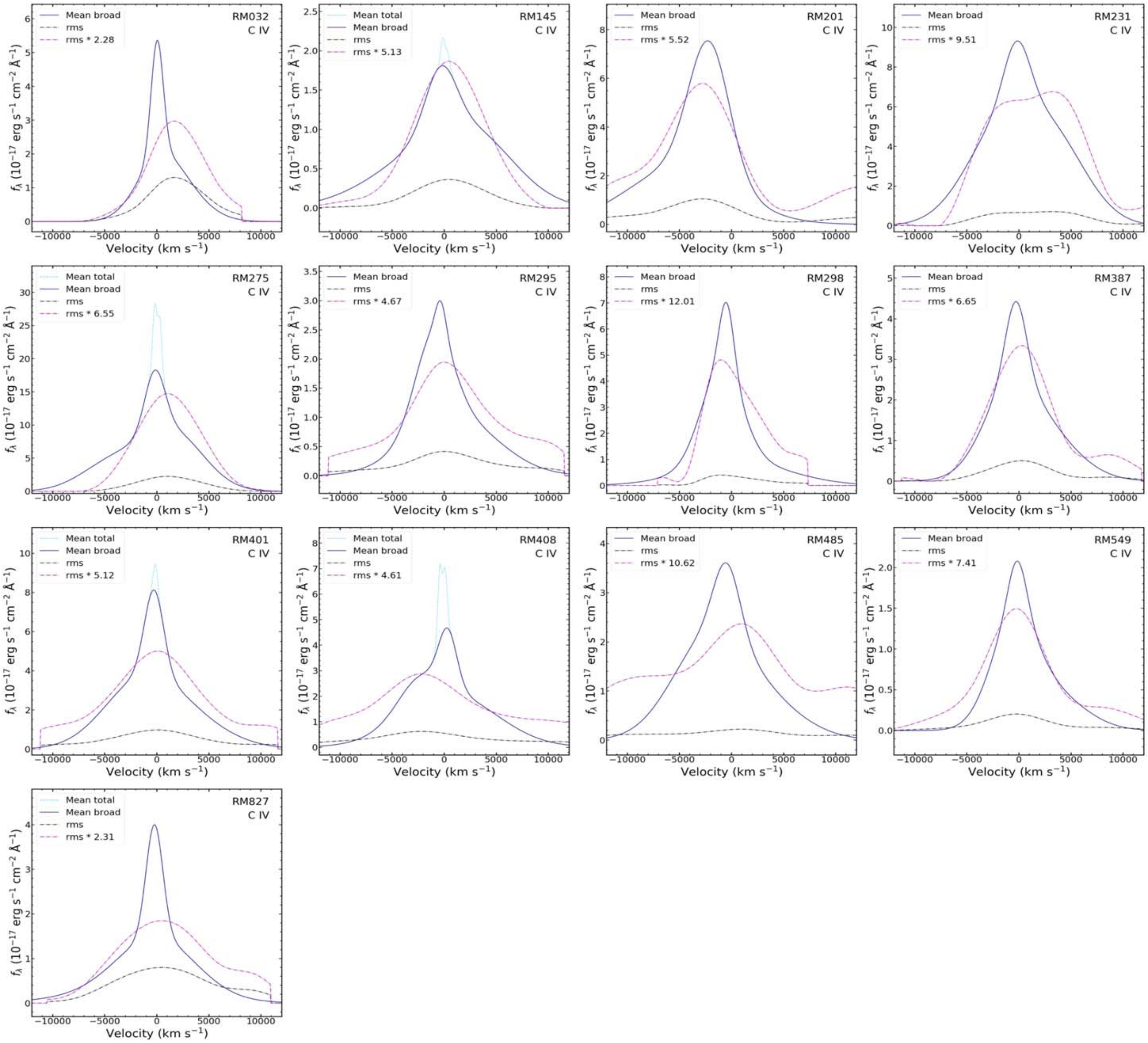

Figure 25. Same as Figure 21 but for C IV. We only show the mean total model if there is evidence for a narrow-line component.

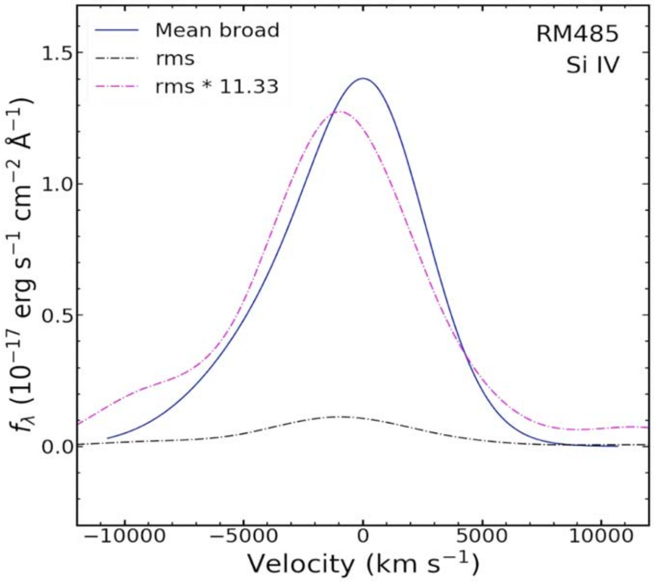

Figure 26. Same as Figure 21 but for Si IV.

ORCID iDs

Shu Wang https://orcid.org/0000-0002-2052-6400
Yue Shen https://orcid.org/0000-0003-1659-7035
Linhua Jiang https://orcid.org/0000-0003-4176-6486
C. J. Grier https://orcid.org/0000-0001-9920-6057
Keith Horne https://orcid.org/0000-0003-1728-0304
Y. Homayouni https://orcid.org/0000-0002-0957-7151
B. M. Peterson https://orcid.org/0000-0001-6481-5397
Jonathan R. Trump https://orcid.org/0000-0002-1410-0470
W. N. Brandt https://orcid.org/0000-0002-0167-2453
P. B. Hall https://orcid.org/0000-0002-1763-5825
Luis C. Ho https://orcid.org/0000-0001-6947-5846
Jennifer I-Hsiu Li https://orcid.org/0000-0002-0311-2812
K. Kinemuchi https://orcid.org/0000-0001-7908-7724
Ian D. McGreer https://orcid.org/0000-0002-3461-5228
D. P. Schneider https://orcid.org/0000-0001-7240-7449

References

Baldwin, J. A. 1977, ApJ, 214, 679
Barth, A. J., Bennert, V. N., Canalizo, G., et al. 2015, ApJS, 217, 26
Barth, A. J., Pancoast, A., Bennert, V. N., et al. 2013, ApJ, 769, 128
Baskin, A., & Laor, A. 2005, MNRAS, 356, 1029
Bentz, M. C., Denney, K. D., Grier, C. J., et al. 2013, ApJ, 767, 149
Blanton, M. R., Bershady, M. A., Abolfathi, B., et al. 2017, AJ, 154, 28
Boroson, T. A., & Green, R. F. 1992, ApJS, 80, 109
Brotherton, M. S., Wills, B. J., Francis, P. J., & Steidel, C. C. 1994, ApJ, 430, 495
Cackett, E. M., & Horne, K. 2006, MNRAS, 365, 1180
Coatman, L., Hewett, P. C., Banerji, M., et al. 2017, MNRAS, 465, 2120
Dawson, K. S., Schlegel, D. J., Ahn, C. P., et al. 2013, AJ, 145, 10
Denney, K. D. 2012, ApJ, 759, 44
Denney, K. D., Peterson, B. M., Dietrich, M., Vestergaard, M., & Bentz, M. C. 2009, ApJ, 692, 246
Dexter, J., Xin, S., Shen, Y., et al. 2019, ApJ, 885, 44
Doi, M., Tanaka, M., Fukugita, M., et al. 2010, AJ, 139, 1628
Eisenstein, D. J., Weinberg, D. H., Agol, E., et al. 2011, AJ, 142, 72
Gaskell, C. M. 1982, ApJ, 263, 79
Gilbert, K. M., & Peterson, B. M. 2003, ApJ, 587, 123
Goad, M. R., Korista, K. T., & Ruff, A. J. 2012, MNRAS, 426, 3086
Goad, M. R., O'Brien, P. T., & Gondhalekar, P. M. 1993, MNRAS, 263, 149
Grier, C. J., Shen, Y., Horne, K., et al. 2019, ApJ, 887, 38
Grier, C. J., Trump, J. R., Shen, Y., et al. 2017, ApJ, 851, 21
Gunn, J. E., Siegmund, W. A., Mannery, E. J., et al. 2006, AJ, 131, 2332
Guo, H., Shen, Y., He, Z., et al. 2020, ApJ, 888, 58
Homan, D., Macleod, C. L., Lawrence, A., Ross, N. P., & Bruce, A. 2020, MNRAS, 496, 309
Homayouni, Y., Trump, J. R., Grier, C. J., et al. 2020, ApJ, 901, 55
Hu, C., Du, P., Lu, K.-X., et al. 2015, ApJ, 804, 138
Hu, C., Wang, J.-M., Ho, L. C., et al. 2008a, ApJL, 683, L115
Hu, C., Wang, J.-M., Ho, L. C., et al. 2008b, ApJ, 687, 78
Hu, C., Wang, J.-M., Ho, L. C., et al. 2012, ApJ, 760, 126
Kelly, B. C. 2007, ApJ, 665, 1489
Kelly, B. C., Bechtold, J., & Siemiginowska, A. 2009, ApJ, 698, 895
Kinney, A. L., Rivolo, A. R., & Koratkar, A. P. 1990, ApJ, 357, 338
Korista, K., Baldwin, J., & Ferland, G. 1998, ApJ, 507, 24
Korista, K. T., & Goad, M. R. 2000, ApJ, 536, 284
Korista, K. T., & Goad, M. R. 2004, ApJ, 606, 749
Kozłowski, S., Kochanek, C. S., Udalski, A., et al. 2010, ApJ, 708, 927
O'Brien, P. T., Goad, M. R., & Gondhalekar, P. M. 1995, MNRAS, 275, 1125
Park, D., Woo, J.-H., Treu, T., et al. 2012, ApJ, 747, 30
Peterson, B. M., Ferrarese, L., Gilbert, K. M., et al. 2004, ApJ, 613, 682
Pogge, R. W., & Peterson, B. M. 1992, AJ, 103, 1084
Proga, D., & Kallman, T. R. 2004, ApJ, 616, 688
Proga, D., Stone, J. M., & Kallman, T. R. 2000, ApJ, 543, 686
Richards, G. T., Kruczek, N. E., Gallagher, S. C., et al. 2011, AJ, 141, 167
Richards, G. T., Vanden Berk, D. E., Reichard, T. A., et al. 2002, AJ, 124, 1
Rumbaugh, N., Shen, Y., Morganson, E., et al. 2018, ApJ, 854, 160
Runco, J. N., Cosens, M., Bennert, V. N., et al. 2016, ApJ, 821, 33
Salviander, S., Shields, G. A., Gebhardt, K., & Bonning, E. W. 2007, ApJ, 662, 131
Shen, Y. 2013, BASI, 41, 61
Shen, Y., Brandt, W. N., Dawson, K. S., et al. 2015a, ApJS, 216, 4
Shen, Y., Brandt, W. N., Richards, G. T., et al. 2016a, ApJ, 831, 7
Shen, Y., Greene, J. E., Ho, L. C., et al. 2015b, ApJ, 805, 96
Shen, Y., Greene, J. E., Strauss, M. A., Richards, G. T., & Schneider, D. P. 2008, ApJ, 680, 169
Shen, Y., Hall, P. B., Horne, K., et al. 2019, ApJS, 241, 34
Shen, Y., Horne, K., Grier, C. J., et al. 2016b, ApJ, 818, 30
Shen, Y., & Kelly, B. C. 2010, ApJ, 713, 41
Shen, Y., & Kelly, B. C. 2012, ApJ, 746, 169
Shen, Y., & Liu, X. 2012, ApJ, 753, 125
Shen, Y., Richards, G. T., Strauss, M. A., et al. 2011, ApJS, 194, 45
Smee, S. A., Gunn, J. E., Uomoto, A., et al. 2013, AJ, 146, 32
Sulentic, J. W., Bachev, R., Marziani, P., Negrete, C. A., & Dultzin, D. 2007, ApJ, 666, 757

Sun, M., Xue, Y., Richards, G. T., et al. 2018, ApJ, 854, 128
Tsuzuki, Y., Kawara, K., Yoshii, Y., et al. 2006, ApJ, 650, 57
Tytler, D., & Fan, X.-M. 1992, ApJS, 79, 1
Vestergaard, M., & Wilkes, B. J. 2001, ApJS, 134, 1
Wang, J., Xu, D. W., & Wei, J. Y. 2018, ApJ, 858, 49
Wang, S., Shen, Y., Jiang, L., et al. 2019, ApJ, 882, 4
Waters, T., Kashi, A., Proga, D., et al. 2016, ApJ, 827, 53
Wilhite, B. C., Vanden Berk, D. E., Brunner, R. J., & Brinkmann, J. V. 2006, ApJ, 641, 78
Wills, B. J., Brotherton, M. S., Fang, D., Steidel, C. C., & Sargent, W. L. W. 1993, ApJ, 415, 563
Yang, Q., Shen, Y., Chen, Y.-C., et al. 2020, MNRAS, 493, 5773
Yue, M., Jiang, L., Shen, Y., et al. 2018, ApJ, 863, 21
Zu, Y., Kochanek, C. S., & Peterson, B. M. 2011, ApJ, 735, 80